Corrosion mechanisms of ferritic-martensitic P91 steel and Inconel 600 nickel-based alloy in molten chlorides. Part II: NaCl-KCl-MgCl2 ternary system

B. Grégoire, C. Oskay, T.M. Meißner, M.C. Galetz

https://doi.org/10.1016/j.solmat.2020.110675

Corrosion mechanisms of ferritic-martensitic P91 steel and Inconel 600 nickel-based alloy in molten chlorides. Part II: NaCl-KCl-$MgCl_2$ ternary system.

B. Grégoire*, C. Oskay, T.M. Meißner, M.C. Galetz*

DECHEMA-Forschungsinstitut, Theodor-Heuss-Allee 25, 60486 Frankfurt am Main, Germany

* Corresponding authors: benjamin.gregoire85@laposte.net (B. Grégoire), mathias.galetz@dechema.de (M.C. Galetz)

ABSTRACT

Molten chlorides are promising heat transfer fluids (HTF) and thermal energy storage (TES) materials for third-generation concentrated solar power (CSP) plants. Despite their low cost and wide operating temperature ranges (400-800°C), structural materials experience severe corrosion in commercially available chloride salts. The understanding of the corrosion mechanisms is therefore critical for successful plant design to ensure constant power generation over the 30 years of expected lifetime. This work investigates the corrosion behavior of ferritic-martensitic P91 steel and Inconel 600 nickel-based alloy in molten NaCl-KCl-$MgCl_2$ (24.5-20.5-55.0 wt.%) under isothermal conditions at 700°C in Ar. For both alloys, the corrosion attack is associated with the selective dissolution of Cr and the removal of Cr-rich carbides from the alloy matrix leaving subsurface voids. The initial "impurity-driven" corrosion mechanism associated with the cathodic reduction of $MgOH^+$ impurities leads to the formation of insoluble MgO on the substrates' surface. Compositional and microstructural features of the alloys, especially the distribution of Cr-rich carbides as well as the solubility and mobility of carbon within the metallic matrix, are found to significantly affect their corrosion resistance. The experimental observations indicate, that the formation of galvanic pairs and solid-state diffusion mechanisms play a major role regarding the corrosion attack of the alloys. The systematic corrosion experiments conducted in this study indicate a lower corrosiveness of NaCl-KCl-$MgCl_2$ ternary mixture than that of NaCl-KCl binary mixture in static conditions at 700°C under Ar. This work gives significant insights into corrosion issues that may be expected in third-generation industrial CSP plants.

Keywords: Concentrated solar power (CSP); Molten salts; Chlorides; Corrosion; Thermodynamics; Kinetics

1. Introduction

Concentrated solar power (CSP) technology has received increasing interest over the past decades as one of the most competitive alternatives to fossil fuels in supplying electricity efficiently while drastically reducing the CO_2 emissions on a global scale [1,2,3]. The principle of CSP systems is to concentrate the solar radiation using programmable mirrors (*heliostats*) onto a so-called receiver where the focused solar energy is converted into thermal energy and stored via heat transfer fluids (HTF) [1,4]. In modern CSP plants such as solar power towers, the primary cycle containing the HTF is combined with a heat exchanger to produce steam in a secondary cycle and drive a conventional steam turbine for power generation [4]. The use of molten salts as HTF and for thermal energy storage (TES) considerably increased the competitiveness of CSP technology by overcoming the intermittency of solar resources. As a matter of fact, the TES system using molten nitrate salts at Gemasolar CSP

plant in Spain (solar power tower operational since May 2011) extended its electricity generation autonomy for up to 15 hours without sunlight [5].

Despite an improved dispatchability for electricity generation, the operating temperature of the state-of-the-art HTF "*solar salt*" (non-eutectic mixture of 60 wt.% $NaNO_3$-40 wt.% KNO_3) is limited to maximum operating temperatures ranging between 560-580°C due to thermal decomposition reactions [6-9]. Since the overall thermodynamic efficiency of a CSP plant is correlated to the maximum operating temperature of the HTF and its liquidus temperature, alternative salt mixtures with appropriate thermophysical properties have been investigated for the next generation of CSP plants [10-13]. Among these alternative salt mixtures, molten chlorides are particularly promising owing to their beneficial characteristics such as low costs, good heat transfer properties and thermal stability up to 800°C [7,8,10,11,12], which offer great prospects to power a supercritical carbon dioxide (s-CO_2) Brayton cycle. The relatively high liquidus temperature of common binary chloride eutectics (e.g. 657°C for NaCl-KCl, 459°C for $MgCl_2$-NaCl or 504°C for $CaCl_2$-NaCl [14]) limits their utilization for industrial applications. Consequently, ternary chloride salt mixtures have been developed to further decrease the liquidus temperature without having a significant effect on the decomposition temperature [10,11,12,15]. Among the different ternary systems investigated, NaCl-KCl-$MgCl_2$ salt mixtures are particularly attractive, as such mixtures possess a wide operating temperatures range, adequate thermophysical properties and are quite inexpensive [12,15,16].

However, structural materials (i.e. iron- and nickel-based alloys) experience severe corrosion in chloride salt mixtures, which renders their use as HTF very challenging [7,8,17-23]. In the event of damage, the costs of replacing the components are further increased by the unscheduled shutdown of the power plant. Therefore, an improved understanding of the prevailing corrosion mechanisms and mitigation strategies are decisive to ensure reliable and consistent power generation for the 30 years expected lifetime of a CSP plant [7,16,22]. It is known that the level of impurities (e.g. moisture, O_2, metallic and oxide impurities or foreign ions) strongly affects the corrosion rates of metallic alloys in chloride melts [17,24,25]. Appropriate measures can therefore be taken to limit the corrosiveness of chloride melts: (i) utilization of an inert atmosphere (e.g. Ar or N_2) as ullage gas, (ii) hindering the introduction of water in the system or include a drying step upon heating of the salt mixture and (iii) purifying the salt mixture before its introduction in the thermal energy storage system. Nevertheless, it is worth mentioning that the operation of a CSP plant requires very large amounts of salt as HTF (e.g. 8500 tons of nitrate salts in Gemasolar CSP plant [5]). The purification of such large amounts of salt at industrial scale with satisfactory results presents several challenges which are still to be overcome and decreases the overall economic viability of using chloride salt mixtures as HTF for the next generation of CSP plants.

Since $MgCl_2$ is highly hygroscopic, this salt is very sensitive to moisture and special care should be taken when handling $MgCl_2$ to limit the absorption of water molecules [7,8,12,26]. In practice, the hydration of $MgCl_2$ at ambient temperature and its further hydrolysis reactions upon heating are unavoidable. The hydrolysis reactions of $MgCl_2$ have been thoroughly investigated using differential thermal analysis (DTA) as well as differential scanning calorimetry (DSC) in the literature and the following reactions may occur upon heating [26,27,28] with the progressive dehydration of hydrated phases:

$$MgCl_2.xH_2O(s) \rightleftarrows MgCl_2.(x-y)H_2O(s) + yH_2O(g) \qquad T \geq 117°C \qquad (1)$$

$$MgCl_2.2H_2O(s) \rightleftarrows MgCl_2.H_2O(s) + H_2O(g) \qquad T \geq 242°C \qquad (2)$$

$$MgCl_2.H_2O(s) \rightleftarrows MgCl_2(s) + H_2O(g) \qquad T \geq 304°C \qquad (3)$$

At about 182°C, the partial hydrolysis of $MgCl_2$ following reaction (4) can also take place [26,27,28]:

$$MgCl_2.2H_2O(s) \rightleftarrows MgOHCl(s) + HCl(g) + H_2O(g) \qquad T \geq 182°C \qquad (4)$$

Upon further heating at temperatures above 350°C and among a wide range of possible reactions the complete hydrolysis of $MgCl_2$ into MgOHCl and its further dehydroxylation above 554°C occur [26,27,28]:

$$MgCl_2.H_2O(s) \rightleftarrows MgOHCl(s) + HCl(g) \qquad T \geq 350°C \qquad (5)$$

$$MgOHCl(s) \rightleftarrows MgO(s) + HCl(g) \qquad T \geq 554°C \qquad (6)$$

Four major problems can therefore be considered upon thermal hydrolysis of $MgCl_2$: (i) the formation of oxidizing $MgOH^+$ impurities through ionic dissociation of MgOHCl, (ii) the formation of magnesium oxide (MgO) within the melt modifying its thermophysical properties, (iii) the progressive loss of $MgCl_2$ implying an alteration of the salt chemistry and of its liquidus temperature and (iv) the requirement to handle the acid gases (i.e. hydrogen chloride, HCl) produced during the reactions. In addition, the acid gases released may accelerate the corrosion of metallic components as reported by Kruizenga [17]. The systematic formation of hydrogen chloride gas during thermal hydrolysis of $MgCl_2$ forces the Deacon reaction (7) to proceed to the right in presence of oxygen (O_2), i.e. generation of chlorine (Cl_2):

$$4HCl(g) + O_2(g) \rightleftarrows 2Cl_2(g) + 2H_2O(g) \qquad (\Delta rG°_{700°C} = 14.3\ kJ/mol) \qquad (7)$$

Reaction (7) illustrates the influence of the ullage gas (i.e. partial pressure of O_2) on the formation of Cl_2. The generation of Cl_2 in the system has a twofold effect: it can accelerate the corrosion of metallic alloys following the generalized reaction (8) and causes serious health hazards, which requires its neutralization with a strong basis (e.g. sodium hydroxide NaOH) before release in the environment.

$$M(s) + x/2\ Cl_2(g) \rightleftarrows MCl_x(s,g) \qquad (8)$$

with M corresponding to one of the metal alloying elements [29].

The detrimental influence of O_2 on the corrosion of metallic alloys in molten chlorides indicates that tolerable corrosion rates in molten chlorides can only be reached in environments with low partial pressure of O_2 such as high-purity Ar or nitrogen (N_2) atmospheres [17,18,19]. In a recent publication, Ding et al. investigated the influence of $MgOH^+$ impurities on the corrosion behavior of Incoloy 800H [30]. The authors developed an electrochemical cell to purify a ternary NaCl-KCl-$MgCl_2$ melt by forcing the reduction of $MgOH^+$ species into insoluble MgO at the cathode, following reaction (9), and the oxidation of Mg into soluble Mg^{2+} cations at the anode, following reaction (10). The overall electrochemical reaction can therefore be written as (11):

$$2MgOH^+ + 2e^- \rightarrow 2MgO(s) + H_2(g) \qquad (9)$$

$$Mg(s) \rightarrow Mg^{2+} + 2e^- \qquad (10)$$

$$2MgOH^+ + Mg(s) \rightarrow 2MgO(s) + Mg^{2+} + H_2(g) \qquad (11)$$

The authors have shown that the corrosion rate of Incoloy 800H was significantly reduced by reducing the level of corrosive $MgOH^+$ impurities [30]. Using atomic absorption spectroscopy (AAS), they analyzed the concentrations of alloying elements Cr, Fe and Ni dissolved in the melts after exposure of Incoloy 800H to molten NaCl-KCl-$MgCl_2$ with and without purification. While Ni was detected neither in purified nor in impurified salts (AAS detection limit of 10 ppm in weight), the concentrations of Cr and Fe dissolved in the melt were higher in the impurified salt compared to that of in the purified salt. In addition, AAS analyses indicated that the concentration of Cr dissolved in the melts is always higher than the one of Fe. This indicates that the reactivity of Ni with the

corrosive species is very low in comparison to Cr and Fe and that Cr is preferentially dissolved. This is in good agreement with the electromotive force (EMF) series in NaCl-KCl-$MgCl_2$ in respect of the apparent standard potential electrodes (given in V vs. Pt^{2+}/Pt at 475°C) of the couples Cr^{2+}/Cr (-1.472), Fe^{2+}/Fe (-1.259) and Ni^{2+}/Ni (-0.868) [31]. Moreover, it also agrees with the standard Gibbs free energy of reaction between MgOHCl and Cr (-106.5 kJ/mol), Fe (-52.9 kJ/mol) and Ni (8.6 kJ/mol) at 700°C following reaction (12) with thermodynamic data from Ref. [32]:

$$2MgOHCl(s) + M(s) \rightarrow 2MgO(s) + MCl_2(s) + H_2(g) \quad (12)$$

with M corresponding to Cr, Fe or Ni.

In a second study [8], Ding et al. concluded that the corrosion mechanisms of various alloys in molten NaCl-KCl-$MgCl_2$ were controlled by electrochemical reactions rather than Cl_2-induced corrosion under Ar atmosphere. The corrosion attack of iron- and nickel-based materials in molten NaCl-KCl-$MgCl_2$ was usually associated with the selective dissolution of Cr resulting in porous Cr-depleted layers of several microns depth from the substrates' surface [7,8,20,21]. The formation of MgOHCl species within NaCl-KCl-$MgCl_2$ melts was identified as the most important factor influencing the corrosion resistance of alloys by Vidal and Klammer [26] as well as Fernández and Cabeza [16]. This was further confirmed in a recent study where different MgOHCl concentrations in a commercial dehydrated carnallite obtained by different purification methods had a clear impact on the corrosion rates of Haynes 230 [33].

In our study, the main objective was to elucidate the corrosion mechanisms in presence of such corrosive impurities and give corrosion rates to what can be considered as an unforeseen event (i.e. incomplete drying and purification process of the salt, rehydration of the salt or unintentional ingress of moisture or oxygen into the system). Ferritic-martensitic P91 steel and Inconel 600 nickel-based alloy were selected for the molten chloride corrosion experiments since both alloys are TES containment material candidates for CSP applications [3]. Following our previous study focusing on the NaCl-KCl binary system [34], the present study investigates the corrosion behavior of P91 steel and Inconel 600 in molten NaCl-KCl-$MgCl_2$ at 700°C under Ar atmosphere for up to 300 h exposure. The influence of testing conditions on the corrosion rates of the alloys is discussed following a probabilistic approach. Related corrosion mechanisms are also presented in light of the experimental observations and thermodynamic considerations.

2. Experimental procedures

2.1. Materials

The nominal and tested chemical compositions of as-received ferritic-martensitic P91 steel (Vallourec) and Inconel 600 (VDM Metals) are compiled in Table 1. Optical emission spectrometry (OES) measurements were performed with a SPECTROMAXx analyzer from SPECTRO Analytical Instruments GmbH (Kleve, Germany). Ferritic-martensitic P91 steel is widely employed in conventional and nuclear power plants and heat exchanger systems with an excellent combination of high temperature creep resistance up to 650°C, high thermal conductivity and good weldability [35,36]. This material has also attracted interest for the development of piping components and storage tanks in CSP plants and offers a cost-efficient alternative to austenitic steels and nickel-based alloys [37,38]. Inconel 600 is an austenitic solution strengthened nickel-based alloy that has been extensively used over the past decades for steam generator tubes in the nuclear industry [39,40]. Owing to its high nickel content and relatively low Cr content, Inconel 600 was also found to present superior corrosion resistance in chloridation-oxidation conditions (i.e. atmospheres rich in chlorine and hydrogen chloride) [41,42] as well as in molten chlorides [17]. The comparison of the corrosion behavior of these two reference industrial alloys is therefore expected to give valuable information for alloy selection and development for CSP applications.

Table 1
Nominal and tested chemical compositions of the two commercial alloys investigated in this study (wt.%). OES: optical emission spectrometry.

Alloy	Composition	Fe	Cr	Ni	Mo	Mn	V	Ti	Si	C	Other
P91 (1.4903)	Nominal	Bal.	8.0-9.5	≤ 0.40	0.85-1.05	0.30-0.60	0.18-0.25	-	0.20-0.50	0.08-0.12	Nb: 0.06-0.10
	OES	89.0	8.7	0.20	0.84	0.43	0.20	-	0.24	0.08	Nb: 0.08
Inconel 600 (2.4816)	Nominal	6.0-10.0	14.0-17.0	Bal.	-	≤ 1.00	-	≤ 0.30	≤ 0.50	≤ 0.15	Cu: ≤ 0.50
	OES	8.3	17.1	73.2	-	0.25	-	0.21	0.40	0.04	Cu: 0.07

As-received P91 and Inconel 600 metallic plates were machined into rectangular samples of, respectively, 25 mm x 6 mm x 3 mm and 25 mm x 5 mm x 3 mm dimensions. The metallic samples were then ground with progressively finer SiC papers (P320, P800 and P1200), washed with distilled water and ultrasonically cleaned in ethanol before any other step. The as-received microstructure of both alloys was characterized before exposure following the same procedure as the one described in Ref. [34]. In Fig. 1a, ferritic-martensitic P91 steel presents a characteristic tempered martensite obtained after normalizing and a subsequent tempering treatment [35,36]. The electrochemical etching highlights the distribution of precipitates at the prior austenite grain boundaries (PAGBs) and at the martensite lath boundaries, corresponding to $M_{23}C_6$ carbides (M: Cr, Mn, Fe, Mo) and fine MX [M: V, Nb and X: C, N] carbonitrides [35,36]. In Fig. 1b, as-received Inconel 600 shows large austenite grains with Cr-rich intergranular carbides formed after solution annealing and rapid cooling [39]. It should be mentioned here that no intragranular carbides were observed within the γ-solid solution matrix of Inconel 600 before exposure.

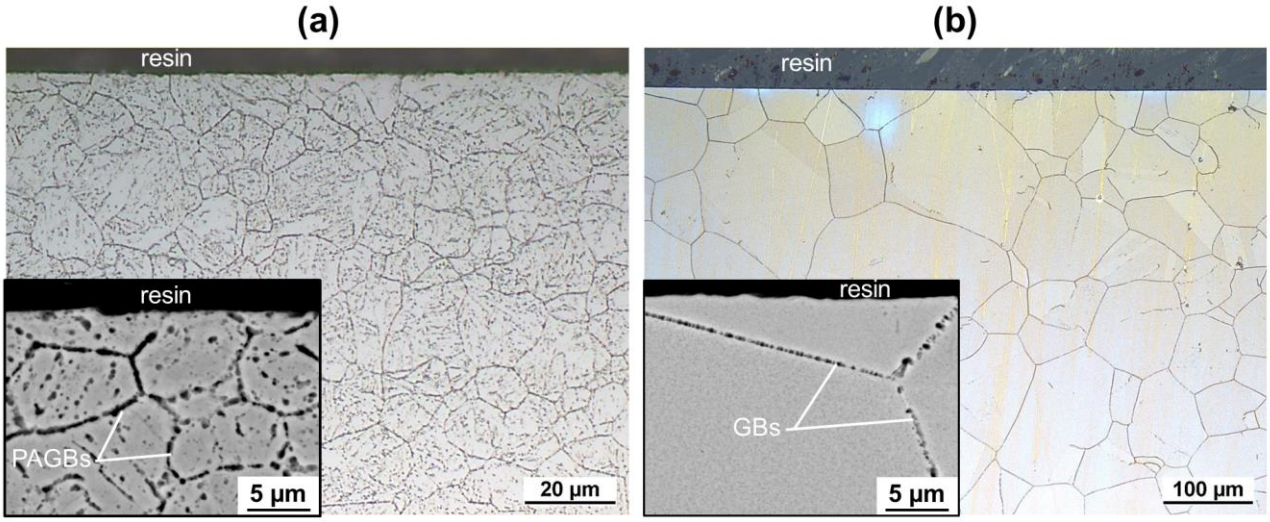

Fig. 1. Light optical cross-section images of as-received (a) ferritic-martensitic P91 steel and (b) Inconel 600 alloy after electrochemical etching with 10% oxalic acid [34]. The corresponding BSE cross-section images at higher magnification are given in the insets. PAGBs: prior austenite grain boundaries, GBs: grain boundaries.

2.2. Corrosion tests in molten salt environment

NaCl, KCl and $MgCl_2$ anhydrous salts (all > 99 wt.% purity) were purchased from Alfa Aesar, Germany. The investigated salt mixture was prepared in hermetic plastic containers by weighing the desired amounts of salts according to the eutectic composition (24.5 NaCl-20.5 KCl-55.0 $MgCl_2$ in wt.%, i.e. 33.0 NaCl-21.6 KCl-45.4 $MgCl_2$ in at.%). The theoretical and experimental eutectic temperatures are, respectively, 383 and 387°C [12,15]. The plastic containers were carefully sealed with a tight moisture-barrier and stored in a desiccator between each use to prevent moisture absorption of the highly hygroscopic $MgCl_2$ salt. However, it should be noted that the initial weighing of the salt was performed in ambient air, which most likely resulted in some water absorption before sealing of the container. This was taken into account in the interpretation of the results. Before exposure, the airtight containers with the salt mixtures were thoroughly mixed for 2 h in a turbular mixer to ensure their homogeneity in composition.

Based on the target temperature for the next generation of CSP plants, the temperature selected for the corrosion experiments was 700°C [20]. All elements in contact with the salt mixture and the metallic samples (i.e. crucibles, lids and rods, see Fig. 2a) were made of alumina to avoid galvanic couples and because of its chemical inertness in molten chlorides [24]. The alumina components were systematically baked in air at 1000°C for 24 h before the corrosion experiments following ISO 17245 [43]. After a final grinding step with P1200 SiC paper, the metallic samples were rinsed with distilled water and ultrasonically cleaned in ethanol. The sample dimensions were then measured with a digital micrometer (mean of 5 different measurements with a maximum deviation of ± 5 µm). The samples were ultrasonically cleaned in ethanol and dried a second time right before embedding in the salt mixture.

As described in Ref. [34] and illustrated in Fig. 2a, the metallic samples were hanged vertically in the alumina crucibles containing approximately 19 g of the eutectic salt mixture. The partial embedding of the samples in the salt mixture enabled the investigation of different regions (e.g. initially immersed in the salt or above the salt immersion level) as shown by Sarvghad et al. [44] and Bell et al. [45]. For each experiment, two samples of each alloy were placed in the hot zone of a horizontal furnace equipped with a quartz tube. After the disposition of the crucibles at room temperature, the furnace was purged with Ar (5 ppm water vapour + 2 ppm O_2) at 12 L/h to

remove the atmospheric contaminants. The Ar flow rate was then decreased to 1.8 L/h before the heating procedure and the absolute pressure of the furnace was maintained slightly above the atmospheric pressure. Following Ding et al. [7,8], the furnace was heated at 5°C/min up to 200°C, held at 200°C for 1 h to remove residual water and further heated at 5°C/min up to 700°C. The temperature was controlled with a Type-S thermocouple and monitored at 700±4°C during the experiment as per ISO 17245 [43]. The isothermal corrosion tests were then carried out at 700°C for 20, 100 and 300 h under an Ar flow of 1.8 L/h.

While a 1 h step at 200°C and a slow heating ramp until melting is acknowledged to fully dry NaCl-KCl mixtures in flowing inert gas without undergoing hydrolysis reactions [54], the presence of $MgCl_2$ drives thermal hydrolysis as described in the sequence reactions (1)-(5). It was previously reported by Ding et al. [46] that the subsequent heating procedure results in a concentration of the corrosive MgOHCl impurity of approximately 2000 ppm in molten NaCl-KCl-$MgCl_2$. Zhao et al. [33] recently demonstrated that commercially available salts such as "dehydrated" carnallite already contains water leading to high concentrations of MgOHCl by hydrolysis in non-treated salts (≥ 5 wt.%). Purification methods including thermal treatment and chemical treatment with metallic Mg can significantly reduce the MgOHCl content in the melt, which offers promising insights to control the corrosiveness of $MgCl_2$-containing salt mixtures for CSP applications providing that these procedures are economically viable [17,26,27,30,33]. As already mentioned in the introduction, the main objective of our study was to elucidate the corrosion mechanisms in presence of such corrosive impurities and give corrosion rates to what can be considered as an unforeseen event (i.e. incomplete drying and purification process of the salt, rehydration of the salt or unintentional ingress of moisture or oxygen in the system). This is an important concern in case of ingress of moisture or oxygen in the system through flanges and valves, which may be expected during CSP plant operation. The presence of MgOHCl corrosive impurities in the system was therefore expected to play an important role in the corrosion mechanisms and to give valuable information on the importance of adequate handling of $MgCl_2$ for large scale industrial applications.

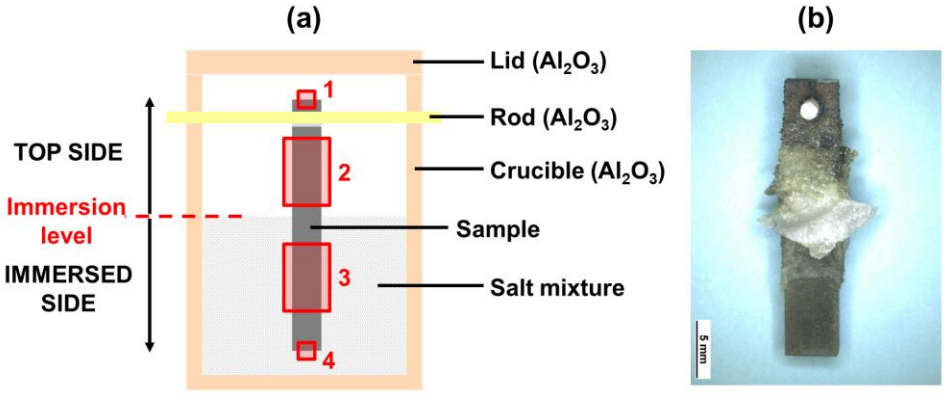

Fig. 2. (a) Schematic representation of the experimental set up used for the molten salt exposure [34] and (b) corresponding macrograph of one Inconel 600 sample after partial embedding in molten NaCl-KCl-$MgCl_2$ for 100 h at 700°C showing the residual salt mixture attached to the sample. The locations 1 to 4 correspond to the areas of investigation with, respectively, 1: top edge, 2: outer region, 3: immersed region and 4: bottom edge.

2.3. Metallographic preparation of the samples after the corrosion tests

Right after the corrosion experiments, the corroded samples were pulled out from the alumina crucibles with special care to preserve salt residues and corrosion products for metallographic observation (see Fig. 2b). The corroded samples were then systematically cold-embedded in epoxy resin by vacuum impregnation to prevent absorption of water molecules and allow cross-section preparation. After curing, a water-free metallographic

preparation using petroleum oil as lubricant [47] was conducted to prevent the dissolution of water-soluble compounds. Grinding was carried out automatically down to P2400 SiC paper followed by a final polishing with 3 µm and 1 µm diamond solutions. Cross-sectioned samples were systematically cleaned with dry acetone containing molecular sieve and dried with hot air. To prevent moisture absorption, especially of the highly hygroscopic $MgCl_2$ compound, the mounted samples were stored in a desiccator. Metallographic observations were carried out on "fresh" cross-sections right after polishing to limit the evolution of the salt mixture associated with the formation of hydrated compounds.

Unlike conventional cleaning methods using acids [7] or deionized water [8,20,21], such a water-free preparation preserves the corrosion products and permits the simultaneous characterization of the salt to examine, for instance, oxide or metal residues. As shown in our previous study [34], the additional information preserved by these means permitted a further understanding of the corrosion mechanisms taking place upon exposure of the metallic materials in chloride melts.

2.4. Dimensional metrology and characterization methods

The determination of the corrosion rates of metallic alloys in molten chlorides is very challenging since oxide scale formation, intergranular attack or metal dissolution may occur simultaneously. In addition, the corrosion front of structural materials in molten chlorides is usually not uniform and depends, among other parameters, on local thermodynamic conditions, on the existence of temperature gradients and on microstructural heterogeneities in the alloys (i.e. precipitates, metallurgical defects). This combination of effects greatly challenges the reliability of gravimetric methods to evaluate the corrosion behavior of structural materials in molten chlorides as reported by other research groups [8,21,45]. It also appears counter-intuitive to give average corrosion rates as a benchmark of the different alloys since local corrosion attacks, such as intergranular attack, may lead to premature failure of structural components at elevated temperatures by stress corrosion cracking (SCC) despite an acceptable average corrosion rate [48,49]. To overcome these limitations, dimensional metrology appears to give satisfactory results by measuring the metal loss of the substrate affected by corrosion with a probabilistic approach following ISO 26146 [50].

Dimensional metrology was initially developed to characterize the corrosion behavior of metallic samples exposed to Type-II hot corrosion experiments due to the complexity of the corrosion processes [51,52,53]. The aim of the dimensional metrology method is to accurately compare the *wall thickness* of the metallic samples before and after exposure to substantiate the extent of metal loss associated with corrosion. Following ISO 26146 [50], the initial sample thickness t_0 was accurately measured with a digital micrometer before exposure. After exposure, the minimum remaining metal thickness t_{rm} unaffected by corrosion (i.e. intergranular attack, metal dissolution or microstructural instability) was measured at x50 magnification with a LEICA DMLA microscope using Imagic IMS software. Up to 100 individual measurements were performed for each area of investigation. The corresponding metal loss (ML) values were then obtained by Eq. (13):

$$ML = (t_0 - t_{rm})/2 \quad (13)$$

The experimental data set was then plotted on probability plots, following ISO 26146 [50], with a total of 200 measurements for each testing condition (two individual samples per alloy and per exposure time). As shown in the first part of this study [34], these probability plots are particularly attractive to depict if the data is fitting a Gaussian distribution (i.e. straight line whose slope corresponds to the standard deviation of the data set). Any

deviation from a straight line indicates a second distribution in the data set and can be interpreted, for example, as pitting, intergranular corrosion or passivation. This statistical approach overcomes the limitations of gravimetric methods and gives reliable corrosion data with a high degree of confidence.

After the molten salt experiments, the residual salt mixtures left in the alumina crucibles were systematically analyzed by X-ray diffraction (XRD) to identify the crystal structures of the compounds formed. To this end, the salt residues were first milled in an agate mortar with a pestle and placed in the diffractometer at ambient temperature. The analyses were performed with a BRUKER D8 Advance diffractometer with LYNXEYE 1D mode in the Bragg-Brentano configuration using Cu $K_{\alpha 1}$ radiation (0.15406 nm). Scanning electron microscopy (SEM) and energy-dispersive X-ray spectroscopy (EDX) analyses were carried out at 20.0 kV with a PHILIPS XL40 microscope equipped with an EDAX detector. For observations in high vacuum, the cross-sectioned samples were coated with a thin conductive layer of graphite. To further assess the composition of oxide compounds, a RENISHAW inVia micro-spectrometer equipped with Nd:YAG (λ_{exc} = 532.0 nm) and He-Ne (λ_{exc} = 632.8 nm) laser sources was used for Raman and fluorescence analyses.

3. Results

3.1. Characterization of the residual salt mixtures after exposure

To identify the different compounds present in the salt mixtures after exposure, a fraction of the salt residues left in each alumina crucible was prepared for XRD analyses. The corresponding XRD patterns obtained after 20, 100 and 300 h exposure to molten NaCl-KCl-$MgCl_2$ at 700°C are given in Fig. 3a (P91) and Fig. 3b (Inconel 600). Regardless of the substrate composition and of the exposure time, similar diffraction patterns were obtained. In addition to the crystal structures of NaCl (Halite, cubic), $MgCl_2$ (trigonal) and $KMgCl_3$ (Perovskite, orthorhombic), hydrated compounds (i.e. Bischofite $MgCl_2.6H_2O$ and Carnallite $KMgCl_3.6H_2O$) were identified. The partial transformation of the salt mixtures into Bischofite and Carnallite, as a consequence of the high hygroscopicity of $MgCl_2$ [54], occurred during the XRD analyses in air after milling of the salt residues. Milling of the salt mixtures and XRD measurement should have been performed in an inert atmosphere to prevent moisture absorption. However, the chosen conditions were more in line with our objective to preserve the salt residues for microstructural characterization since the transfer of the samples between a desiccator and the characterization methods will always result in some water absorption by $MgCl_2$. This highlights the precautions needed at industrial scale to handle the very large amount of salts required for CSP plant operation and the pressure on adequately performing the drying and/or purification process before introduction of the salt mixture in the system (i.e. storage tanks).

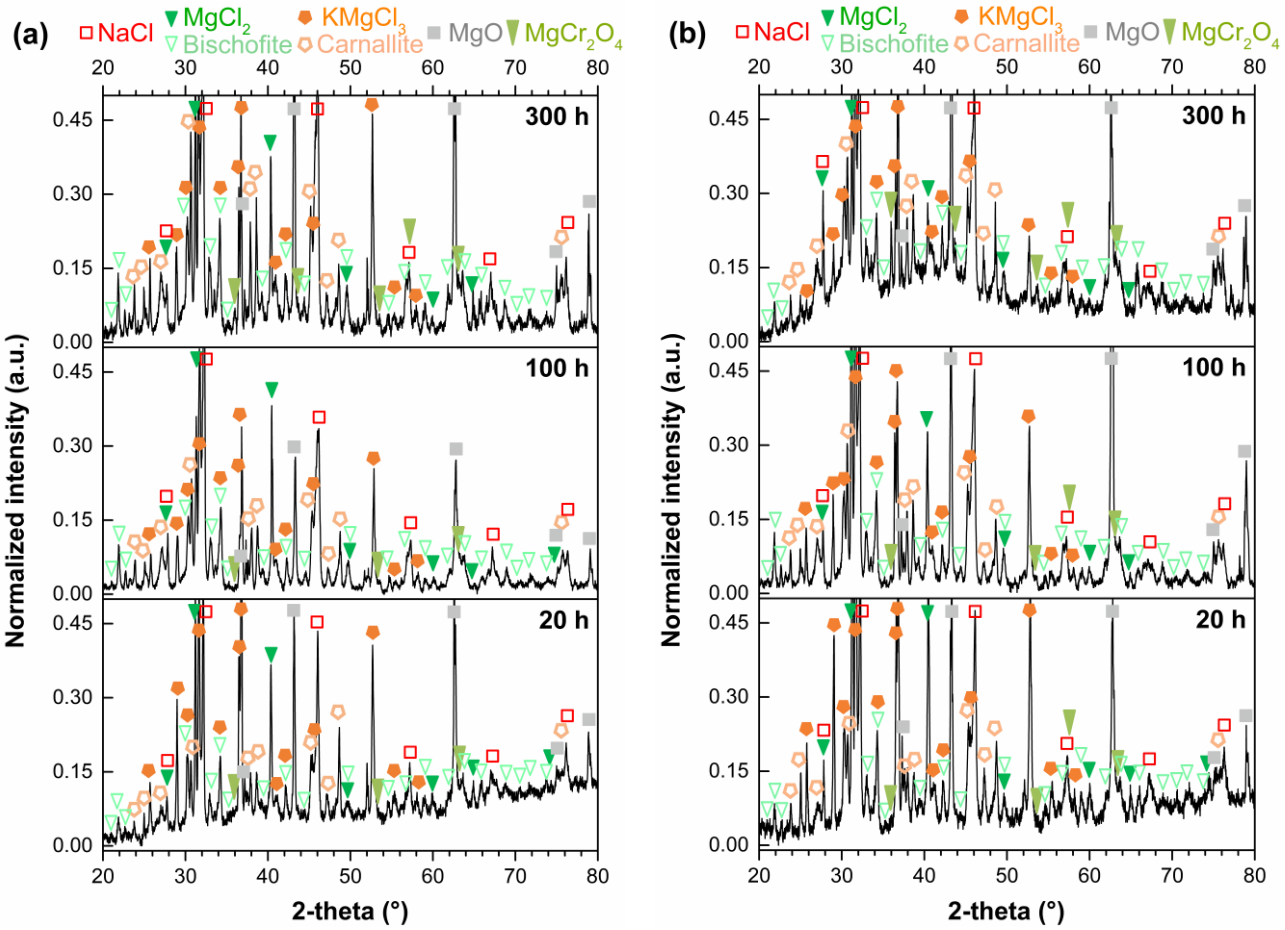

Fig. 3. X-ray diffraction patterns of the salt residues obtained after exposure of (a) P91 and (b) Inconel 600 to molten NaCl-KCl-$MgCl_2$ at 700°C in flowing Ar for 20, 100 and 300 h. Bischofite: $MgCl_2.6H_2O$ and Carnallite: $KMgCl_3.6H_2O$.

In addition to salt compounds, the cubic crystal structure of MgO was systematically identified in the diffraction patterns (Fig. 3a and b) with diffraction peaks at 2θ values of 37.2° (111), 43.2° (200), 62.6° (220), 75.0° (311) and 78.9° (222). Additional diffraction peaks were associated to the cubic structure of magnesiochromite (i.e. $MgCr_2O_4$) with its main diffraction peaks at 35.9° (311), 43.5° (400), 53.6° (422), 57.3° (333) and 63.0° (440). The formation of MgO and of $MgCr_2O_4$ within the salt mixtures by confirmed with SEM observations (Fig. 4). It is worth mentioning, that $MgCr_2O_4$ appearing brighter than MgO in BSE mode was systematically enveloping MgO crystals on the outer region (Fig. 4a and c). This experimental observation is of utmost importance and will serve as a basis to explain the mechanisms of formation of $MgCr_2O_4$ spinel by synergistic dissolution in section 4.3. Whereas quite pure NaCl crystals were randomly formed after cooling (Fig. 4d), the remaining salt mixture was rich in Cl, Mg, K and O suggesting the formation of $KMgCl_3$ and of hydrated compounds (i.e. Bischofite and Carnallite). These observations are in good agreement with the existence of the $KMgCl_3$-NaCl eutectic transformation at about 405°C [55] upon cooling of a ternary NaCl-KCl-$MgCl_2$ salt mixture. In Fig. 4c and d, a decohesion between the salt mixture and the other compounds (i.e. MgO, $MgCr_2O_4$ and NaCl) is systematically observed. This may be related to a volume change of the salt in the vacuum of the SEM chamber before observation (i.e. the hydrated compounds may have released water molecules upon vacuum). Such observations indicate that extreme care must be taken to observe samples containing the highly hygroscopic $MgCl_2$ salt. In some regions of the salt mixture as shown in Fig. 4b, Ni-rich particles can be observed within the MgO crystals. The chemical composition of these particles (1.5Cr-0.5Mn-4.1Fe-93.9Ni in wt.% according to EDX spot measurements) indicates that Cr, Mn and Fe were preferentially depleted by comparison with Inconel 600 (Table 1). It seems that these Ni-rich particles facilitate the growth of

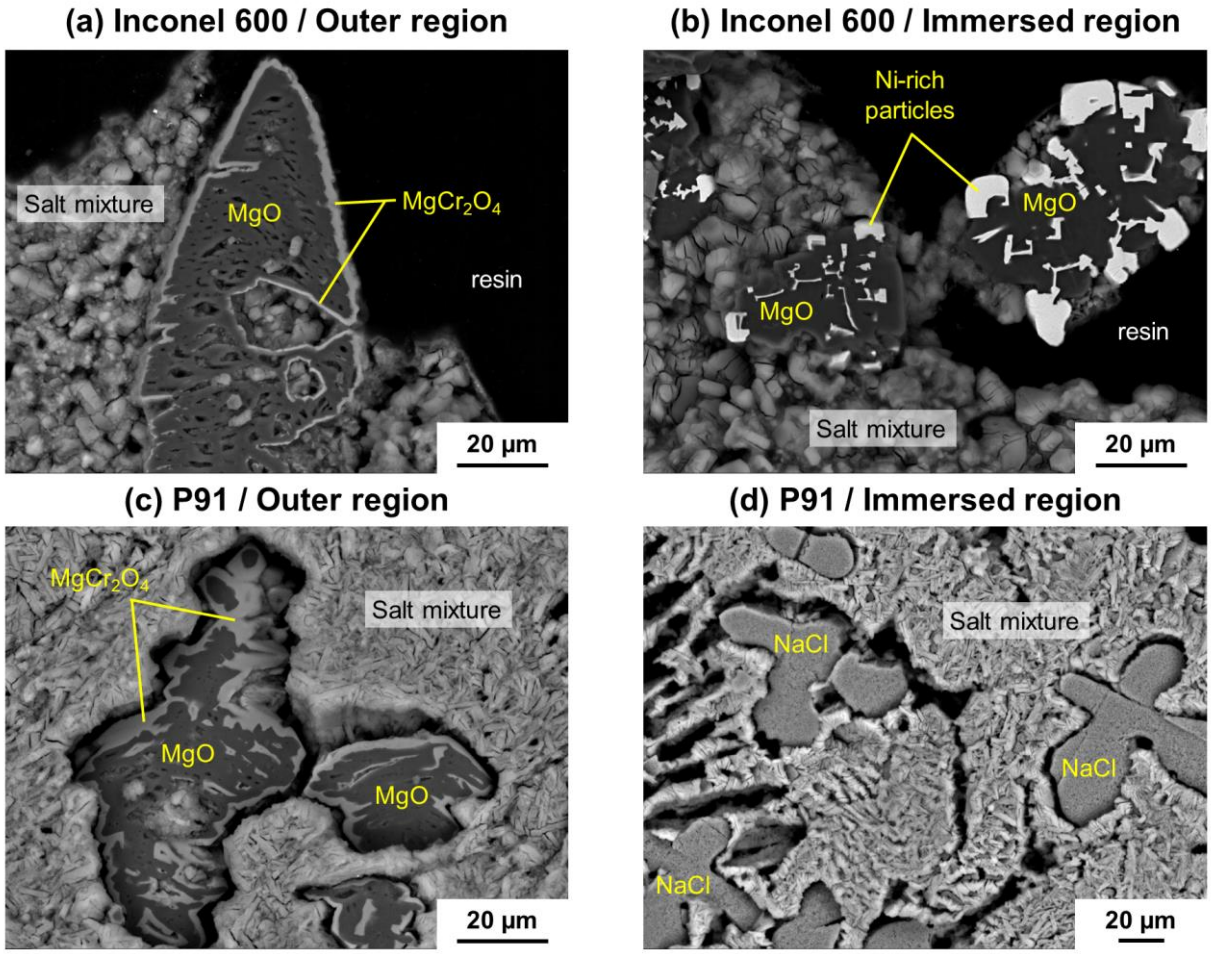

Fig. 4. BSE cross-section images taken in representative areas of the residual salt mixtures after (a), (b) 100 h exposure of Inconel 600 and (c), (d) 300 h exposure of P91 to molten NaCl-KCl-$MgCl_2$ at 700°C in flowing Ar. Refer to Fig. 2a for the selected regions.

MgO, i.e. for the cathodic reduction of oxidizing $MgOH^+$ species following reaction (9) as previously reported by Ding et al. on a tungsten cathode [30].

3.2. Metal loss measurements and corrosion rates

The metal loss measurements of P91 ferritic-martensitic steel and Inconel 600 nickel-based alloy after exposure in molten NaCl-KCl-$MgCl_2$ at 700°C are reported as probability plots in Fig. 5a and b following ISO 26146 [50]. Regardless of the substrate and of the exposure time, the metal loss values are systematically greater on the top side (i.e. above the salt immersion level) than on the immersed side (i.e. below the salt immersion level) of the samples. For each data set, the fraction of the surface enduring pitting corrosion can be estimated from the probability plots as a deviation from a Gaussian distribution (i.e. straight line with a slope corresponding to the standard deviation of the data set) towards higher metal loss values [50]. Whereas Inconel 600 was not prone to pitting corrosion in all testing conditions, up to 4 % of the surface of P91 steel showed pitting corrosion after 20 h exposure (Fig. 5a). This value decreases to about 2-3 % for P91 after 100 and 300 h exposure on the top side. For P91 steel, a maximum corrosion attack of 130 µm was measured after 300 h exposure (Fig. 5a). Despite the fact that Inconel 600 is not prone to pitting corrosion, the probability plots indicate that this substrate is, overall, more sensitive to corrosion in molten NaCl-KCl-$MgCl_2$ than P91 steel. A maximum corrosion attack of 145 µm was measured for Inconel 600 after 300 h exposure (Fig. 5b).

To illustrate the corrosion behavior of the two alloys, cross-section light optical micrographs were taken at different magnifications and are given in Fig. 5c and d after 300 h exposure to molten NaCl-KCl-$MgCl_2$ at 700°C. Extreme care was taken during the water-free preparation of the samples to preserve the corrosion scales and the residual salt mixture attached to the samples. As shown in the low magnification micrographs in Fig. 5c and d, the salt mixture covers the entire surface of the metallic samples after exposure. This most likely indicates that the salt melt wetted all surfaces of the partially-embedded samples. As detected by XRD (cf. Fig. 3), oxide scales are observed within the salt and at the interface between the salt and the metallic substrate. The micrographs at higher magnification were taken in representative areas of the samples to highlight the corroded regions of the substrates associated with void formation (Fig. 5c and d). As observed on the probability plots, the extent of the corrosion attack was, overall, greater on Inconel 600 than on P91 steel, which seems to contradict recent literature data on molten chloride corrosion of iron- and nickel-based alloys. The reasons for the lower corrosion resistance of Inconel 600 compared to P91 steel in static conditions will be discussed in section 4.4.

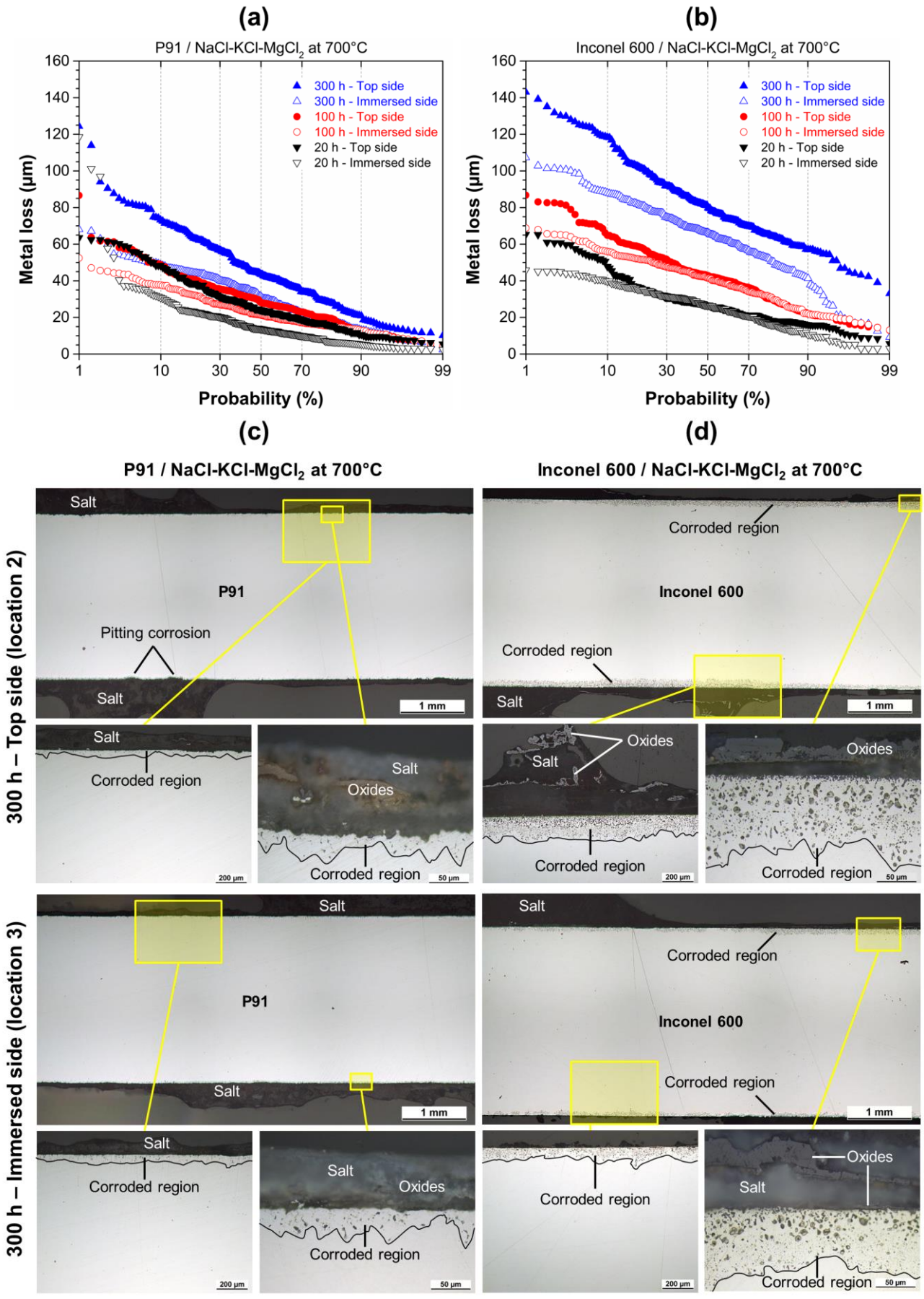

Fig. 5. Probability plots of the metal loss values of (a) P91 and (b) Inconel 600 substrates after exposure to molten NaCl-KCl-$MgCl_2$ at 700°C in flowing Ar and (c), (d) corresponding cross-section light optical micrographs after 300 h exposure. Please note the varying magnifications in cross-section images. The readers are referred to Fig. 2a for the selected locations.

As described in ISO 26146 [50], the median metal loss and corresponding standard deviation values were determined from the probability plots presented in Fig. 5a and b. The results are summarized in Fig. 6a and b (solid columns) and compared with the metal loss data obtained after exposure to molten NaCl-KCl in the first part of this study (hatched columns). As aforementioned, both P91 steel and Inconel 600 show higher metal loss values on the top side than on the immersed side after exposure to the ternary mixture. This was also observed after exposure of P91 to the NaCl-KCl binary mixture (Fig. 6a). On the contrary, the opposite feature was noticed for Inconel 600 when exposed to the NaCl-KCl binary mixture since the largest metal loss values were recorded on the immersed side (Fig. 6b). The standard deviation values are particularly large for P91 samples exposed to molten NaCl-KCl after 100 and 300 h exposure. As shown in Ref. [34], the large spread in metal loss values can be correlated to pitting corrosion in the form of large pits (up to 500 µm deep) after 300 h of exposure. Nevertheless, Inconel 600 is overall more sensitive to corrosion than P91, in particular in the ternary salt mixture. Regardless of the metallic substrate, the metal loss values were significantly lower after exposure in the ternary mixture than in the binary one. This counterintuitive observation indicates that the presence of the hygroscopic compound $MgCl_2$ in the salt mixture, subjected to hydrolysis reactions, does not necessarily result in higher corrosion rates than mixtures which do not contain this compound. The reasons behind the lower corrosiveness of NaCl-KCl-$MgCl_2$ melt than NaCl-KCl melt in static conditions will be one of the subjects of the discussion. However, it should be remembered that these experiments were performed in static conditions and that such effects may not be necessarily transferred to thermal cycling conditions or in a dynamic salt flow by combined erosion effects.

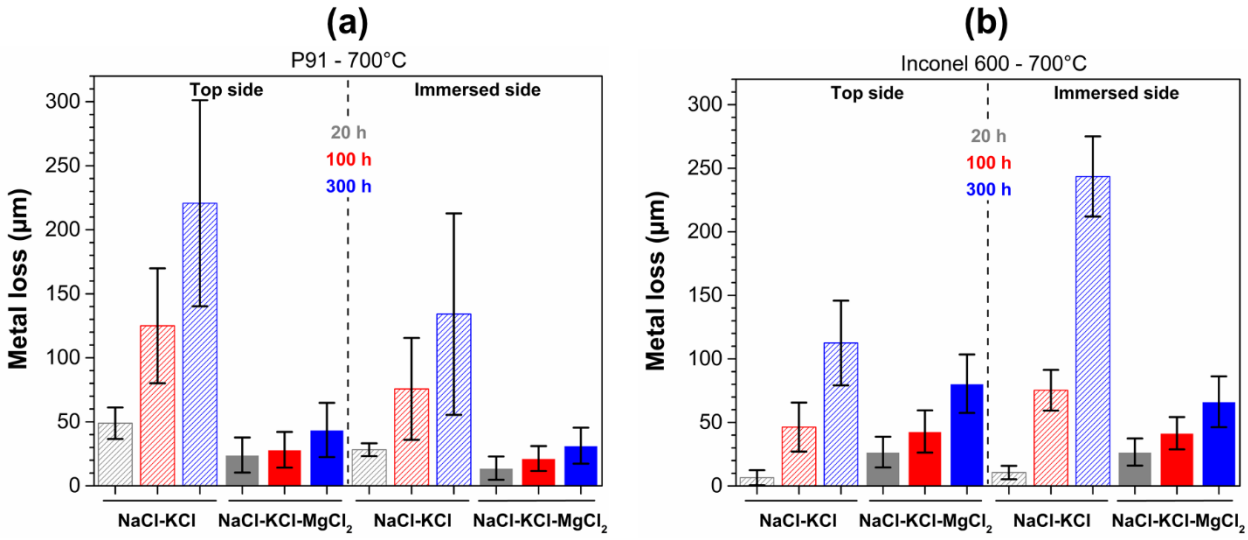

Fig. 6. Summary of median metal loss measurements with standard deviation for (a) P91 and (b) Inconel 600 materials after 20, 100 and 300 h exposure to molten NaCl-KCl (data from Ref. [34]) or to molten NaCl-KCl-$MgCl_2$ at 700°C in flowing Ar.

To compare the corrosion behavior of alloys in different testing conditions, corrosion rates are commonly expressed in µm/year. Therefore, the corrosion rates of both P91 and Inconel 600 alloys exposed to molten NaCl-KCl-$MgCl_2$ at 700°C were calculated on the immersed side and on the top side from the iso-probability curves of metal loss values as a function of exposure time (Fig. 7). For each iso-probability curve, the points indicate the experimental data and the lines the best fit curves following the power-law model [34,56]:

$$ML = k.t^n + c \quad (14)$$

where n is the exponential coefficient and c an empirical constant (in this study $c = 0$). In this study, the n value was adjusted empirically to fit the median values with a precision of ± 0.05 and then kept constant to fit the other iso-probability curves. Despite the empirical nature of this model, the probabilistic approach followed in this study enables sound estimates of variability with regard to corrosion of the two investigated alloys. In addition, the n value gives a good approximation of the physical observations where $n < 0.5$ corresponds to a protective behavior, $n = 0.5$ to a purely Fickian diffusion process (i.e. parabolic-law), $0.5 < n < 1$ to a non-protective behavior, $n = 1$ to a linear corrosion process and finally to breakaway corrosion when $n > 1$.

For all testing conditions and for both alloys (Fig. 7), n values are all < 0.5, which indicates a relatively protective behavior. Nevertheless, the corrosion rates calculated from the 5%, median and 95% iso-probability curves are not acceptable regarding the requirements for industrial applications (≈ 15-30 µm/year based on a components' lifetime target of 30 years [3,8,22]). As aforementioned, P91 steel is more resistant than Inconel 600 to molten NaCl-KCl-$MgCl_2$ at 700°C with both smaller n values and lower corrosion rates (see Fig. 7). Notwithstanding the alloy composition and the initial boundary conditions (top side or immersed side), the iso-probability curves depict initially high corrosion rates in the first 20 h of exposure and, later, steady-state corrosion rates, which is characteristic of impurity-driven corrosion mechanisms [49,57]. As reported by Ding et al. [7,8] and other research groups [16,26,33], this can be associated with the formation of corrosive $MgOH^+$ impurities upon thermal hydrolysis of $MgCl_2$. It should also be noted, that the calculated corrosion rates are systematically higher on the

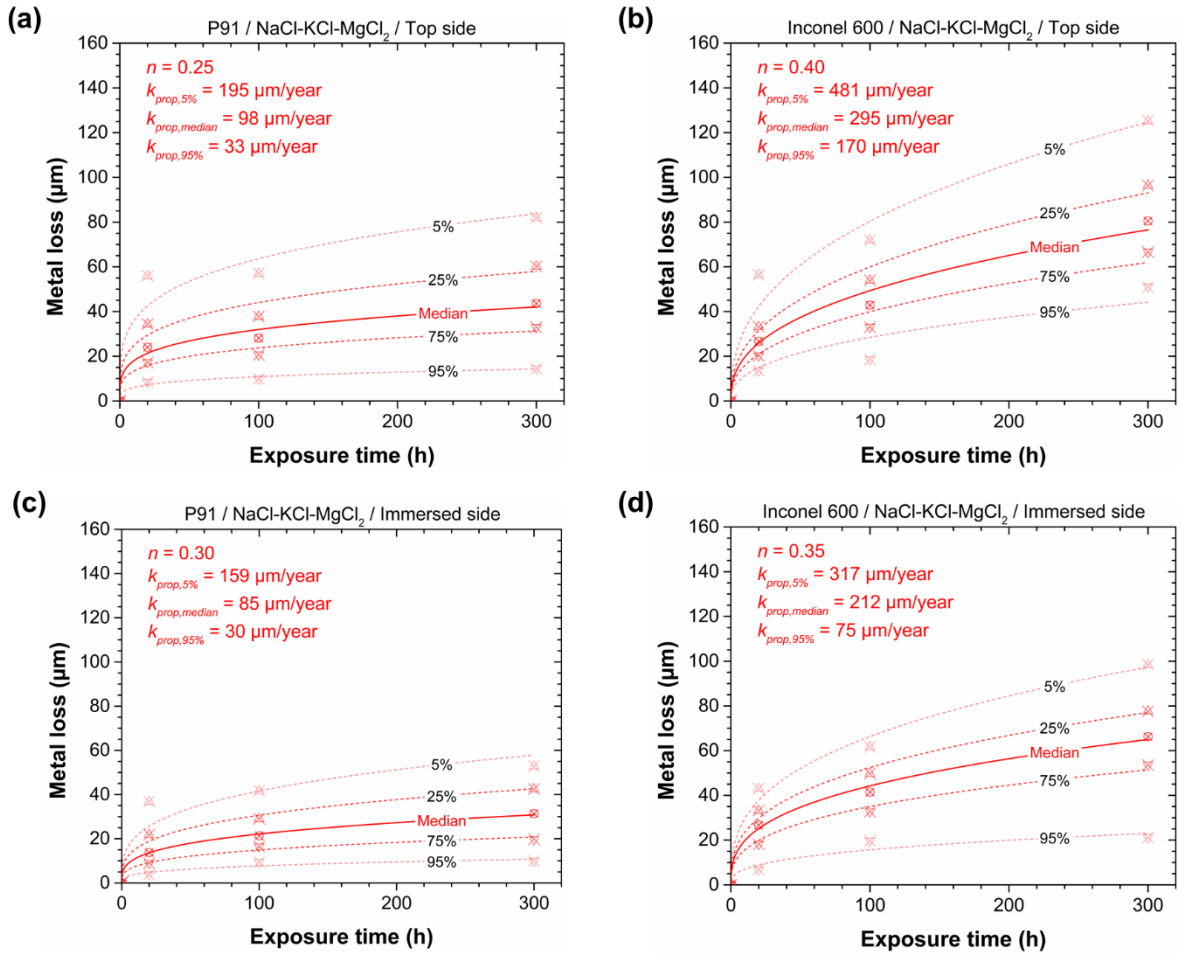

Fig. 7. Iso-probability curves of metal loss values as a function of exposure time for (a), (c) P91 and (b), (d) Inconel 600 alloys exposed to molten NaCl-KCl-$MgCl_2$ at 700°C in flowing Ar. (a), (b) top side corresponds to location 2 in Fig. 2a and (c), (d) immersed side corresponds to location 3 in Fig. 2a. Points indicate experimental data and lines the best fit curves. For each testing condition, the n values as well as the estimated propagation rates corresponding to 5%, median and 95% iso-probability curves are reported on the graphs.

top side (Fig. 7a and b) than on the immersed side (Fig. 7c and d) for both alloys, which may indicate the effect of oxygen availability on the corrosion mechanisms. These effects will be discussed in section 4.2.

3.3. Microstructural characterization of the samples after exposure to molten NaCl-KCl-$MgCl_2$ at 700°C

3.3.1. Ferritic-martensitic P91 steel

The P91 samples exposed to the NaCl-KCl-$MgCl_2$ ternary composition were further characterized by SEM. In Fig. 8, BSE cross-section images taken in representative areas of the samples are presented after 20, 100 and 300 h of exposure. For all investigated areas, relatively continuous MgO scales appearing dark in BSE mode are

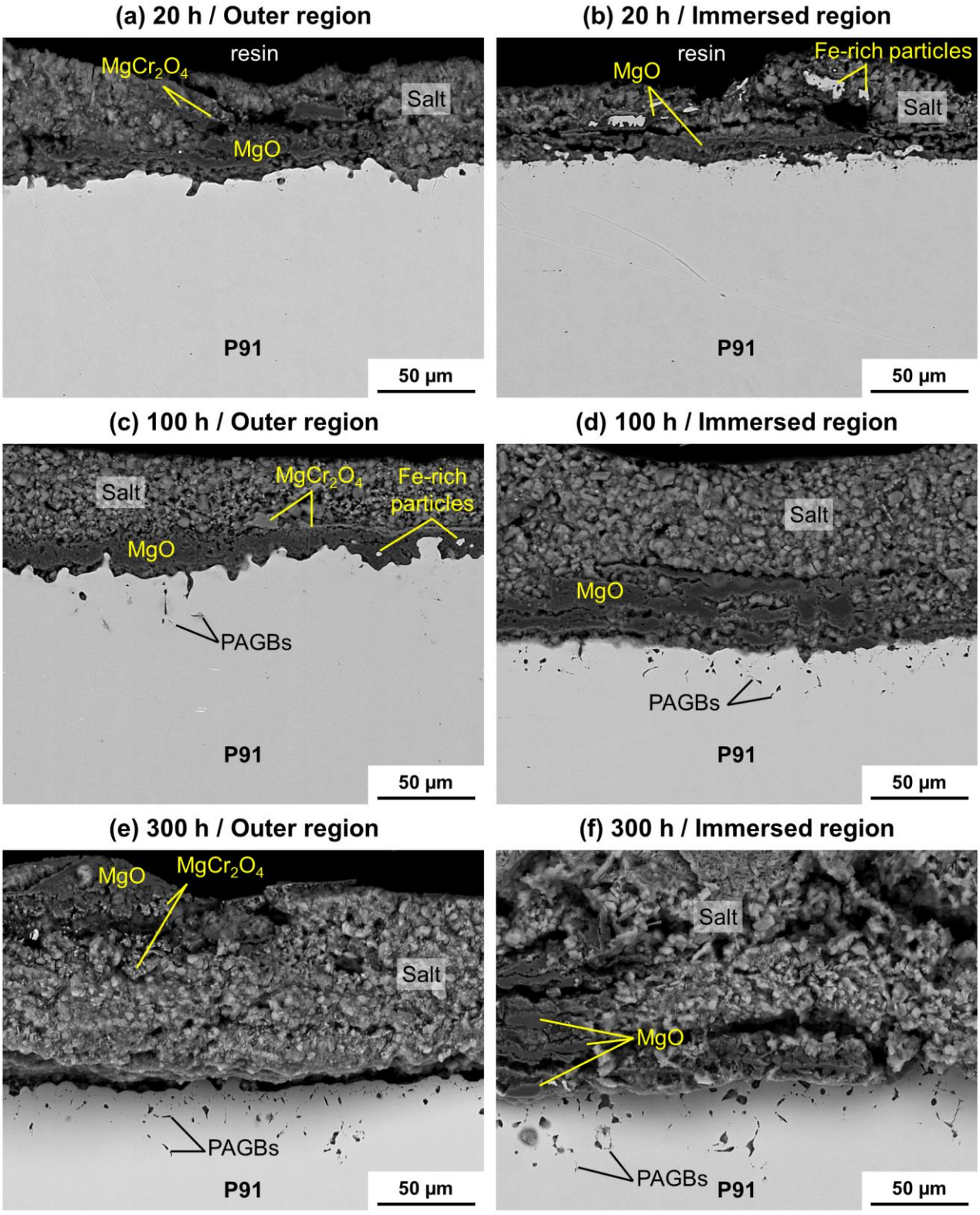

Fig. 8. BSE cross-section images of P91 after (a), (b) 20 h, (c), (d) 100 h and (e), (f) 300 h exposure to molten NaCl-KCl-$MgCl_2$ at 700°C in flowing Ar taken in representative regions of the samples. The readers are referred to Fig. 2a for the selected regions.

observed at the substrate/salt interface. To a lower extent, porous $MgCr_2O_4$ scales, with an intermediate contrast in BSE mode, are also observed on the outer region of the samples (Fig. 8a, c and e). It is worth mentioning, that traces of Si, V, Mn and Fe (total amount < 2 wt.%) were also detected by EDX analyses within $MgCr_2O_4$ scales. Raman micro-spectrometry was used to ascertain the composition of the oxide scales and Fig. 9 presents the representative spectra obtained when analyzing MgO and $MgCr_2O_4$ scales. In MgO scales, the characteristic fluorescence signal of Cr^{3+} ions was systematically detected with a total of ten emission bands including the R and N lines, three band-pairs (α_r, α_b; β_r, β_b; γ_r, γ_b) and the weak band $2\beta_r$ corresponding to the double of the frequency separation between the sharp R line and β_r [58]. Further information is given in Appendix with the expected position of the fluorescence bands calculated from the work of Deutschbein [58] and their experimental observation for both He-Ne laser (632.8 nm) and Nd:YAG laser (532.0 nm). When analyzing $MgCr_2O_4$ scales, the three main vibrational bands of magnesiochromite spinel at 542, 605 and 684 cm^{-1} were successfully identified [59,60]. However, the R and N lines associated with the fluorescence of $MgO:Cr^{3+}$ are also observed in such locations indicating that the porous scales identified as the magnesiochromite spinel are, in fact, a mixture of MgO and $MgCr_2O_4$.

Despite the relatively protective behavior of the MgO scales formed at the substrate/salt interface, grain boundary attack is unambiguously observed on the BSE cross-section images of Fig. 8. As observed in molten NaCl-KCl [34], the corrosion propagates at the prior-austenite grain boundaries (i.e. PAGBs) formed during the heat treatment of P91 steel carried out to confer its mechanical strength [35,36]. This results in the selective removal of Cr-rich carbides from the tempered martensitic microstructure. Furthermore, Fe-rich metallic particles are embedded in the oxide scales on Fig. 8b and c. The low Cr content of such particles, < 1 wt.% Cr according to EDX spot measurements, suggests that some Cr-depleted grains of the substrate became loose upon exposure. After 300 h of exposure (Fig. 8e and f), the metallographic observation of the oxide scales was challenged by the high hygroscopicity of the salt mixture and, most likely, of $MgCl_2$ leading to the formation of hydrated compounds such as bischofite and carnallite as observed by XRD (Fig. 3). The absorption of water molecules from the samples after metallographic preparation and their subsequent desorption while vacuuming the SEM chamber induce volume

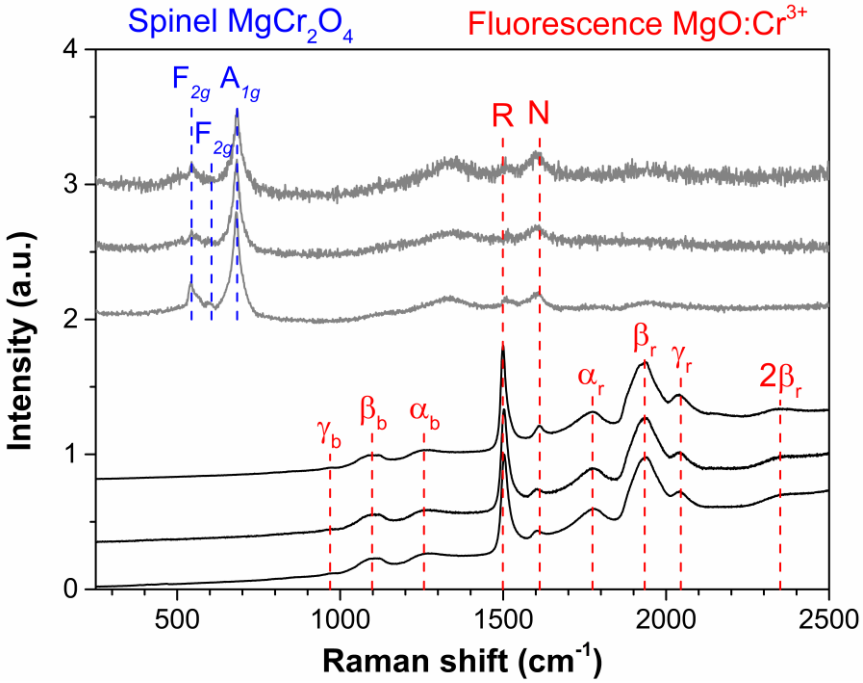

Fig. 9. Raman signal of magnesiochromite ($MgCr_2O_4$) and fluorescence of Cr^{3+} in MgO (λ_{exc} = 632.8 nm) in the oxide scales formed on P91 after 20 h exposure to molten NaCl-KCl-$MgCl_2$ at 700°C in flowing Ar. See Appendix for the identification of the fluorescence bands of the $MgO:Cr^{3+}$ system.

changes, which may be responsible for the difficulties of observation. Nevertheless, it is also possible that the formed MgO scale loses its relatively protective behavior over time, for instance with the build-up of stresses within the growing scale, which might lead to crack formation and/or spallation and thus provide easy access of the electrolyte towards the metallic substrate.

Additional cross-section images of P91 samples after 20 h exposure to molten NaCl-KCl-$MgCl_2$ at 700°C are presented in Fig. 10. At higher magnification, it appears that the MgO scales were undoubtedly in contact with the underlying substrate at temperature. Lateral decohesion observed at the substrate/scale interface (gap filled with either resin (Fig. 10a, b and d) or salt (Fig. 10c)), most likely resulted from mechanical stresses developed upon cooling due to the mismatch of thermal expansion coefficients and due to volume changes during solidification of the salt mixture. Alternatively, such decohesion can also be attributed to the metallographic preparation of the samples including cold-embedding by vacuum impregnation and cross-section polishing. On the outer region of the samples (Fig. 10a and c), $MgCr_2O_4$ spinel appearing with an intermediate contrast in BSE was observed within the MgO scales. Interestingly, longitudinal cracks can be observed at the interface between MgO and $MgCr_2O_4$ spinel. As aforementioned, these cracks may be a consequence of the high CTE mismatch between MgO (≈10.4x10^{-6} K^{-1} at 25°C [61]), P91 steel (≈10.5x10^{-6} K^{-1} at 25°C [62]) and $MgCr_2O_4$ spinel (≈5.7x10^{-6} K^{-1} at 25°C [63]) inducing high compressive stresses on $MgCr_2O_4$ spinel upon cooling of the samples. As observed in Fig. 8, intergranular

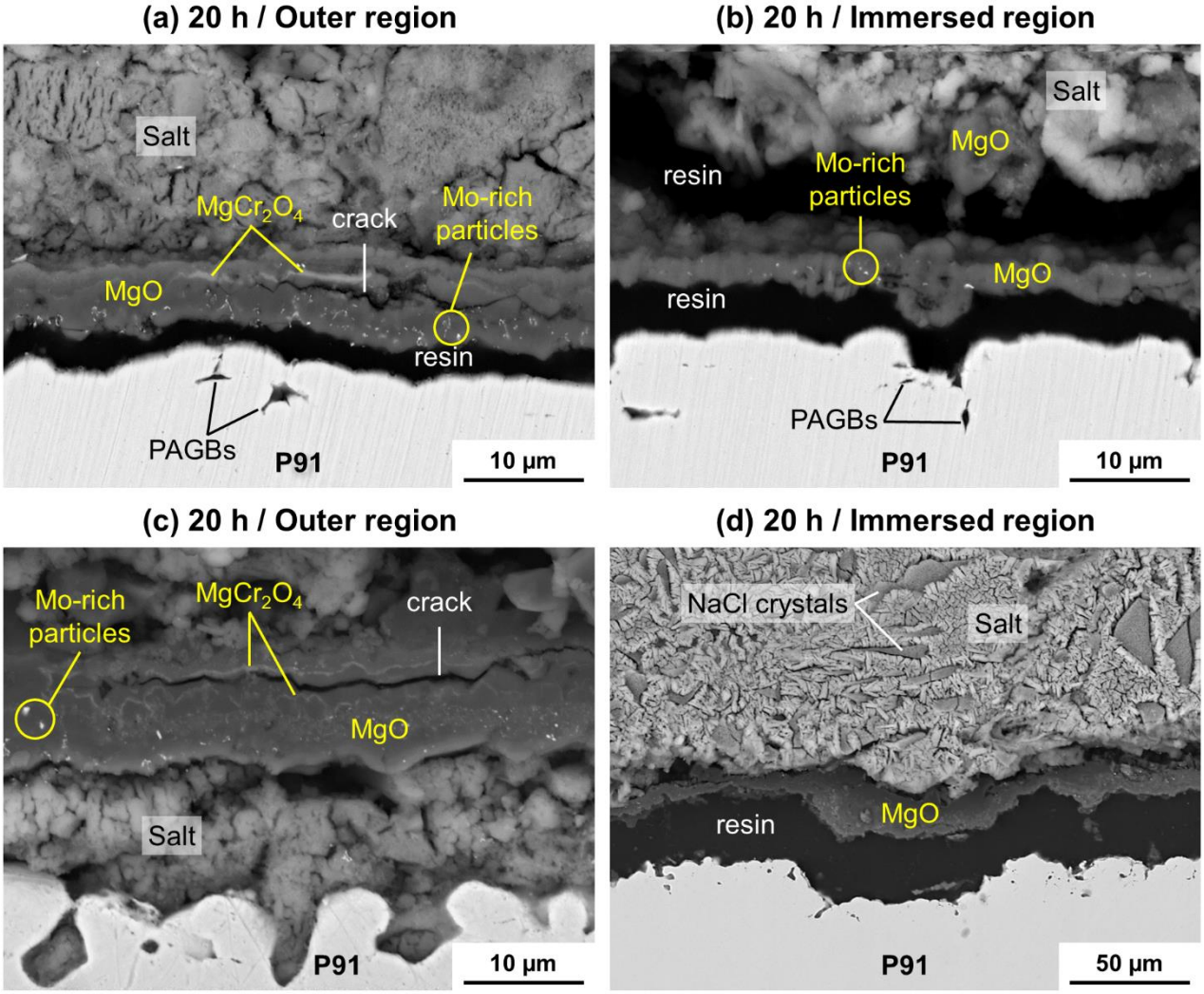

Fig. 10. BSE cross-section images of P91 after 20 h exposure to molten NaCl-KCl-$MgCl_2$ at 700°C in flowing Ar taken in representative regions of the samples. (a), (c) outer region initially above the salt (location 2) and (b), (d) immersed region initially embedded in the salt mixture (location 3).

attack located at the prior-austenite grain boundaries (PAGBs) is visible to a depth of several microns. In addition, fine Mo-rich particles, appearing bright in BSE, are distributed within the MgO scales in Fig. 10a, b and c.

3.3.2. Inconel 600 nickel-based alloy

Whereas relatively continuous and adherent MgO scales formed on P91 (Fig. 8), MgO crystals surrounded with $MgCr_2O_4$ are found to be dispersed in the salt mixture for Inconel 600 (Fig. 11). The SEM observations indicate that

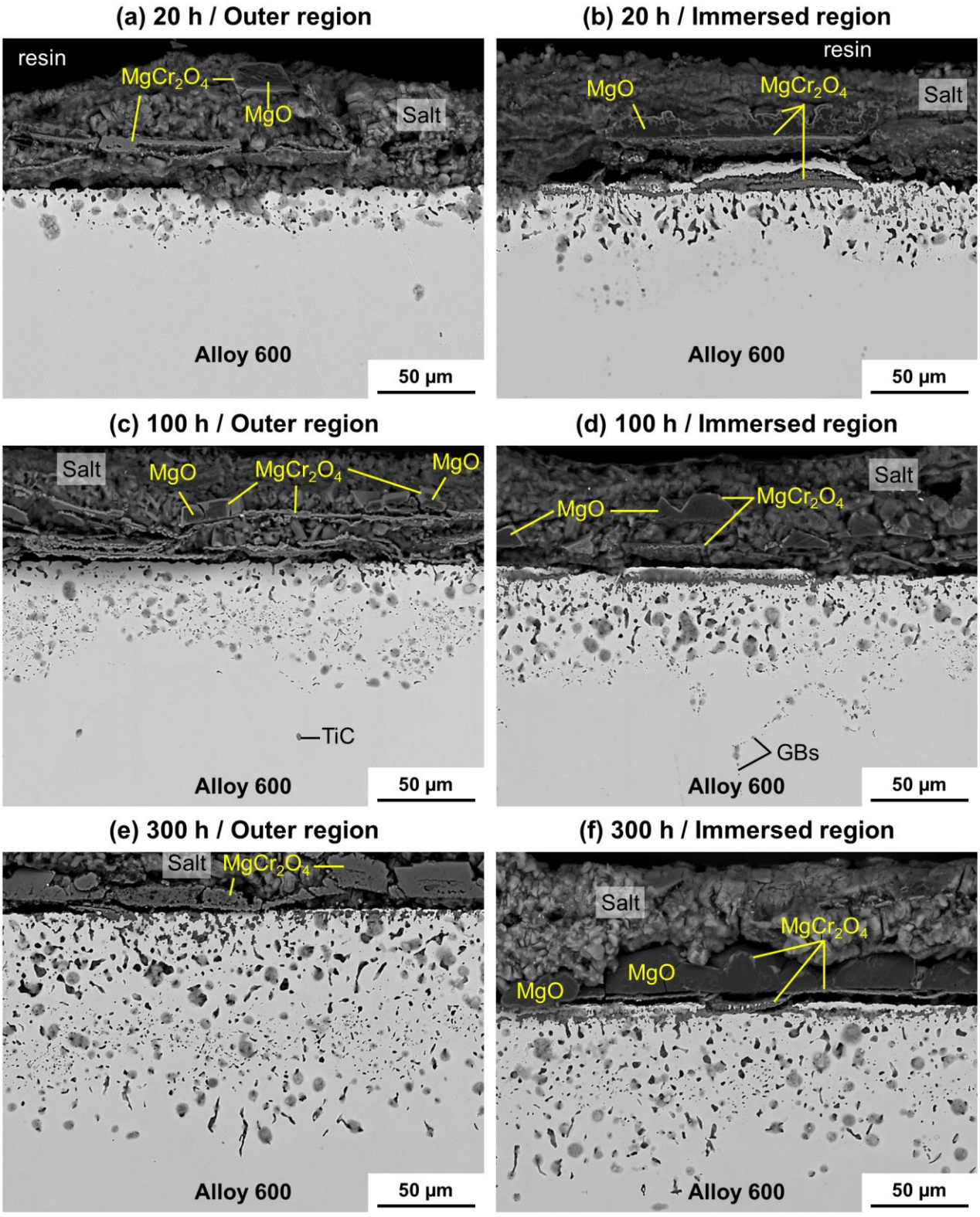

Fig. 11. BSE cross-section images of Inconel 600 after (a), (b) 20 h, (c), (d) 100 h and (e), (f) 300 h exposure to molten NaCl-KCl-$MgCl_2$ at 700°C in flowing Ar taken in representative regions of the samples. The readers are referred to Fig. 2a for the selected regions.

the volume fraction of $MgCr_2O_4$ in the salt is larger on the outer region (Fig. 11a, c and e) than on the immersed region (Fig. 11b, d and f). As commonly observed after exposure of nickel-based alloys to molten chlorides [7,19,20,21,34,64], the corrosion attack resulted in a porous microstructure depleted in Cr (i.e. average concentration of Cr < 4 wt.% according to EDX spot analyses in the alloy matrix). The increasing depth of the corrosion attack over time, associated with a porous morphology, exceeds 80 µm after 300 h exposure (Fig. 11e and f), which indicates the poorly protective behavior of the oxide scales that are unable to inhibit the corrosion attack. Whereas the corrosion attack propagated through the grains of the Inconel 600, grain boundary attack is also observed, for instance, in Fig. 11d. Since Cr-rich carbides were only present at the grain boundaries before exposure (see Fig. 1b), these observations imply that microstructural changes occurred within the γ-(Ni) solid solution matrix of Inconel 600 over time and that secondary phases formed during isothermal exposure at 700°C.

BSE cross-section images at higher magnification are given in Fig. 12 after 300 h exposure. As aforementioned, the corrosion attack resulted in a porous morphology where corrosion products precipitated in the subsurface pores to a depth of about 20 µm in the outer region of the sample (Fig. 12a). EDX spot analyses were performed in such pores and the mean concentration of the main elements was 58.8O-1.8Si-18.6Mg-2.1Ti-15.1Cr-0.5Fe-1.9Ni in at.%. This suggests the presence of both MgO and $MgCr_2O_4$ within the pores as detected by XRD by Ding et al. after 500 h exposure of In800H at 700°C in molten NaCl-KCl-$MgCl_2$ [7]. The detection of higher-valence elements than

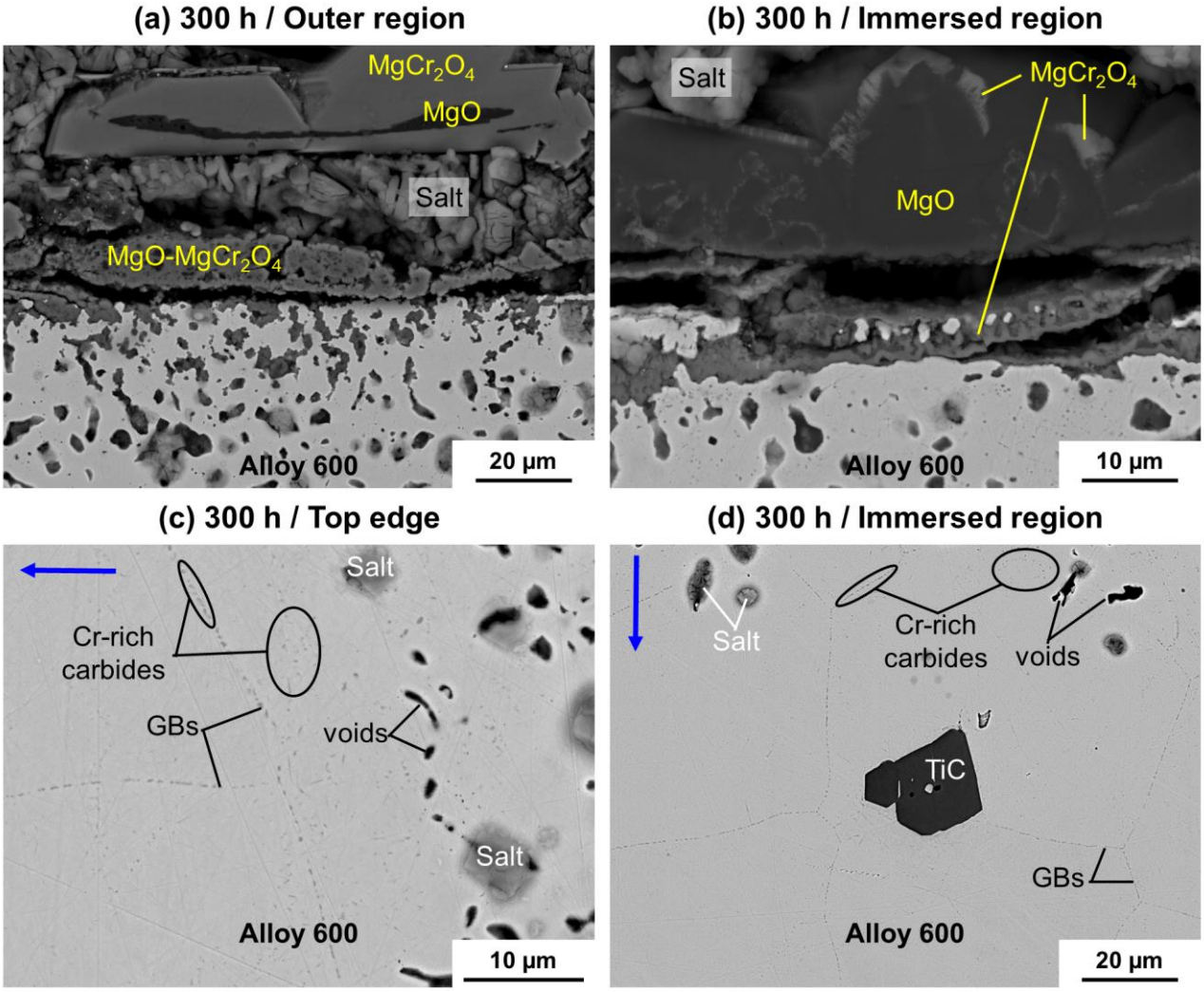

Fig. 12. BSE cross-section images of Inconel 600 after 300 h exposure to molten NaCl-KCl-$MgCl_2$ at 700°C in flowing Ar taken in representative regions of the samples. (a) outer region initially above the salt (location 2), (b), (d) immersed region initially embedded in the salt mixture (location 3) and (c) top edge of the sample (location 1). Arrows in (c), (d) indicate the propagation direction of the corrosion attack.

Cr (i.e. Si and Ti) may indicate the formation of $MgSiO_3$, as observed after 500 h exposure of stainless steel 310 at 700°C in molten NaCl-KCl-$MgCl_2$ in the same study [7], or $MgTiO_3$ perovskites. Nevertheless, complementary characterization techniques should be employed to ascertain these presumptions. Whereas both MgO and $MgCr_2O_4$ compounds were present in the corrosion products on the substrate surfaces, the fraction of $MgCr_2O_4$ was significantly higher in the outer region (Fig. 12a) than on the immersed region (Fig. 12b). This most likely highlights the influence of O_2 availability (i.e. the partial pressure of oxygen) on the mechanisms of formation of $MgCr_2O_4$. These mechanisms will be presented in section 4.3.

Despite the differences in composition of the corrosion products, similar observations can be made within the alloy at the corrosion front (Fig. 12c and d). In fact, the microstructural instability of Inconel 600 at 700°C led to the precipitation of semi-continuous Cr-rich carbides at the grain boundaries and, most importantly, within the grains (i.e. intragranular carbides). The precipitation of Cr-rich carbides within the γ-(Ni) solid solution matrix of Inconel 600 was systematically observed below the corrosion front, as reported in the first part of this study [34] and by other research groups on various nickel-based alloys [45,65]. The propagation of the corrosion attack resulted in the progressive loss of the austenitic grain microstructure of Inconel 600 together with void formation as observed in Fig. 11. The metallographic observations strongly support the hypothesis, that the Cr-rich carbides were selectively dissolved from the γ-(Ni) solid solution matrix, leading to the formation of voids. It is worth mentioning, that salt particles are randomly distributed within the voids/pores (Fig. 12c and d). Since no water was employed during the metallographic preparation of the samples to prevent dissolution of the salt, this indicates that the chloride melt was penetrating through the scales and entering the pores in the metal through capillary effects as proposed by Bell et al. [45].

4. Discussion

4.1. Impurity-driven corrosion mechanisms: role of corrosive $MgOH^+$ impurities

The iso-probability corrosion curves presented in Fig. 7 follow a particular trend associated with "impurity-driven" corrosion [49,57]. As presented in Fig. 13, this is characterized by a transition between initially high corrosion rates within the first hours of exposure to steady-state corrosion rates when the concentration of impurities decreased to negligible amounts and/or when the corrosion becomes driven by a different mechanism [49]. Considering the NaCl-KCl-$MgCl_2$ ternary mixture, the oxidizing $MgOH^+$ impurities resulting from the hydrolysis reactions of $MgCl_2$ upon heating (see reactions (4) and (5)) were identified as the most important oxidant by Ding et al. [7,8] and other groups [16,26,33]. The cathodic reaction of oxidizing $MgOH^+$ impurities into MgO on metallic alloys, following reaction (15), implies an opposite anodic reaction to maintain electric charge neutrality. The latter is therefore associated with metal dissolution from the substrate (see Fig. 13), with the potential electrode series in molten chlorides of the main constituting elements being in the order Cr^{2+}/Cr < Fe^{2+}/Fe < Ni^{2+}/Ni [31]. Cr is then selectively dissolved from the substrate whereas Ni dissolution will be very limited and can thus be disregarded. This results in the partial anodic reactions (16) and (17) for Cr and Fe, respectively. Therefore, the impurity-driven corrosion mechanisms represented in Fig. 13 can be summarized with the overall electrochemical reactions (18) and (19).

Partial cathodic reaction:

$$2MgOH^+ + 2e^- \rightarrow 2MgO(s) + H_2(g) \quad (15)$$

Partial anodic reactions:

$$Cr \rightarrow Cr^{2+} + 2e^- \quad (16)$$

$$Fe \rightarrow Fe^{2+} + 2e^- \quad (17)$$

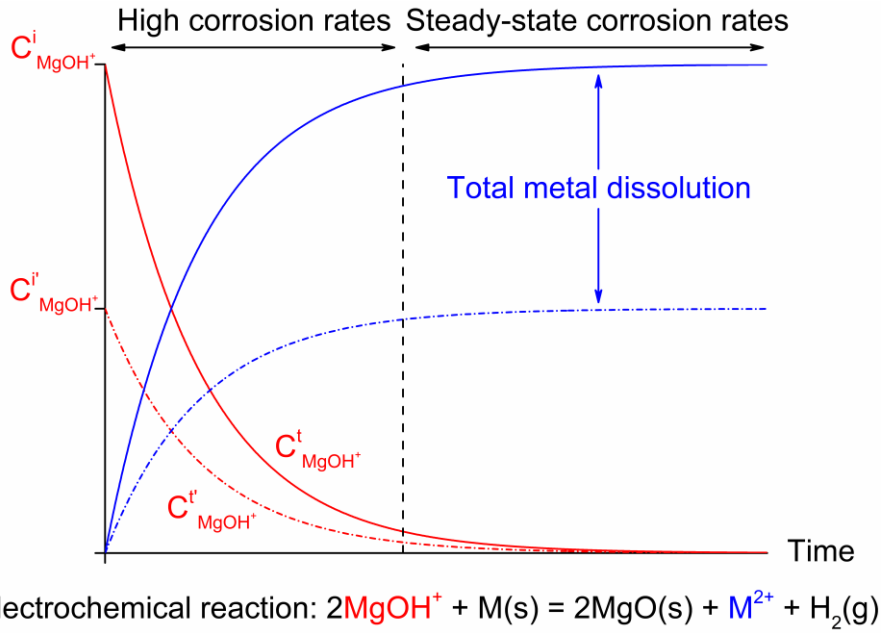

Fig. 13. Schematic representation of the correlations between the concentration of corrosive $MgOH^+$ impurities in the melt and the corrosion rates of metallic alloys as a function of time following the impurity-driven corrosion mechanism. This illustration is based on the electrochemical measurements carried out by Ding et al. in Ref. [30]. C^i: Initial concentration of $MgOH^+$ after heating and C^t: Concentration of $MgOH^+$ as a function of time. The dashed lines represent the case with a lower initial concentration of $MgOH^+$ within the melt.

Overall corrosion reactions:

$$2MgOH^+ + Cr(s) \rightarrow 2MgO(s) + Cr^{2+} + H_2(g) \quad (18)$$

$$2MgOH^+ + Fe(s) \rightarrow 2MgO(s) + Fe^{2+} + H_2(g) \quad (19)$$

Following reaction (15), the reduction of $MgOH^+$ impurities on the substrates' surface should lead to the formation of MgO and H_2. As a matter of fact, MgO was systematically observed on the surface of P91 and Inconel 600 after exposure to molten NaCl-KCl-$MgCl_2$ (see Fig. 8, Fig. 10 and Fig. 11), as previously shown by Ding et al. [7,8] and other groups [19,21] on various iron- and nickel-based alloys. As a result of the progressive formation of MgO on the surface of the metallic substrates and because of the low solubility of MgO in molten chlorides [45], the latter results in the formation of a physical barrier between the molten salt and the metallic substrate, as observed in Fig. 10. After initially high corrosion rates, the reduction of $MgOH^+$ impurities into quite dense and continuous MgO scales decreases the diffusion rates of the corrosive species from the melt towards the substrate. Because MgO possesses a low electrical conductivity at 700°C ($\sigma \approx 10^{-11}$ $\Omega^{-1}.cm^{-1}$ [66]), this results in a relatively protective behavior of the MgO scales in static conditions by decreasing the charge-transfer rates between the melt and the metallic alloys. Similar observations were reported by Ding et al. when exposing stainless steel 310, Incoloy 800H and Hastelloy C-276 to NaCl-KCl-$MgCl_2$ with 1 wt.% Mg addition [8]. The addition of 1 wt.% Mg was indeed promoting the formation of dense and continuous MgO scales on top of the substrates thereby increasing the corrosion resistance of the alloys (corrosion rates decreasing by a factor of 3 for Incoloy 800H and of 16 for Hastelloy C-276 with addition of Mg). Because of a great concentration gradient, H_2 released by reaction (15) is less likely to accumulate within the scales and is continuously swept away by the carrier gas (i.e. Ar flow).

4.2. Influence of O_2 availability on the corrosion mechanisms

To maintain charge neutrality, the formation of metallic cations at the metal/electrolyte interface resulting from the partial anodic reactions (16) and (17) will provoke the electromigration of Cl^- anions towards the metal surface and their reaction following reactions (20) and (21):

$$Cr^{2+} + 2Cl^- \rightarrow CrCl_2(s,g) \quad (20)$$

$$Fe^{2+} + 2Cl^- \rightarrow FeCl_2(s,g) \quad (21)$$

Even though $CrCl_2$ and $FeCl_2$ compounds are less stable than NaCl, KCl and $MgCl_2$ at 700°C, they possess high vapor pressures and their continuous evaporation takes place at the corrosion front [29], leaving voids within the material (see Fig. 10 and Fig. 12). The volatile chloride compounds then diffuse from the metal surface towards the electrolyte through cracks and pores of the oxide scales and other diffusion paths. As described in the widely accepted active-oxidation process [29,42,67,68], the oxygen partial pressure increases gradually within the scale towards the scale/electrolyte interface and, depending on local thermodynamic conditions (see Fig. 14), the gaseous chlorides can react with dissolved oxygen forming porous oxide scales and Cl_2 following reactions (22)-(25):

$$2CrCl_2(g) + \frac{3}{2}O_2(g) \rightleftarrows Cr_2O_3(s) + 2Cl_2(g) \quad (\Delta_rG°_{700°C} = -502.5\ kJ/mol) \quad (22)$$

$$FeCl_2(g) + \frac{1}{2}O_2(g) \rightleftarrows FeO(s) + Cl_2(g) \quad (\Delta_rG°_{700°C} = -22.5\ kJ/mol) \quad (23)$$

$$3FeCl_2(g) + 2O_2(g) \rightleftarrows Fe_3O_4(s) + 2Cl_2(g) \quad (\Delta_rG°_{700°C} = -242.3\ kJ/mol) \quad (24)$$

$$2FeCl_2(g) + \frac{3}{2}O_2(g) \rightleftarrows Fe_2O_3(s) + 2Cl_2(g) \quad (\Delta_rG°_{700°C} = -196.3\ kJ/mol) \quad (25)$$

Even though all reactions (22)-(25) are thermodynamically favored at 700°C (i.e. $\Delta rG° < 0$), the stability of gaseous chlorides will depend on the local O_2 partial pressure as depicted in Fig. 14. Despite the evidence for both Cr and Fe dissolution from immersed P91 samples (Fig. 8 and Fig. 10), only a small fraction of Fe (< 0.5 at.% according to EDX spot measurements) was detected within $MgCr_2O_4$ scales. In addition, the investigation of the salt mixture did not reveal the presence of iron oxides (see XRD analyses in Fig. 3 and SEM observations in Fig. 4). This suggests that the O_2 partial pressure within the melt was too low to significantly oxidize $FeCl_2$ and that $FeCl_2$ was continuously evaporating from the scale to the melt while MgO was progressively formed on the surface. However, a partial pressure of about 10^{-32} atm. is sufficient to form Cr_2O_3 at 700°C and, as observed within the corrosion products and the salt mixture, this led to the formation of $MgCr_2O_4$ spinel together with MgO. The formation of magnesiochromite is thermodynamically favored at 700°C:

$$MgO(s) + Cr_2O_3(s) \rightleftarrows MgCr_2O_4(s) \qquad (\Delta_rG°_{700°C} = -31.7\ kJ/mol) \qquad (26)$$

The fraction of $MgCr_2O_4$ spinel within the corrosion products was significantly larger on the outer region of the samples, i.e. initially above the immersion level of the salt (see Fig. 2a), and more typically for Inconel 600 (Fig. 11a, c and e). Since O_2 is introduced in the system by the Ar flow (2 ppm impurities in the Ar bottle according to the furnisher), its dissolution in the melt and diffusion towards the metal is expected to be faster when a thin layer of salt is formed (creeping of the salt above the immersion level of the salt) than when a large reservoir of salt is present (bottom edge of the sample deep in the salt). It can therefore be concluded that the mechanisms of formation of $MgCr_2O_4$ are intrinsically linked with the availability of O_2 and will be further discussed in section 4.3. In addition to reacting with gaseous metal chlorides, O_2 is also expected to increase the cathodic activity following reaction (27), thereby increasing the electrochemical dissolution rate of Cr from the alloy.

$$O_2(g) + 4e^- \rightarrow 2O^{2-} \qquad (27)$$

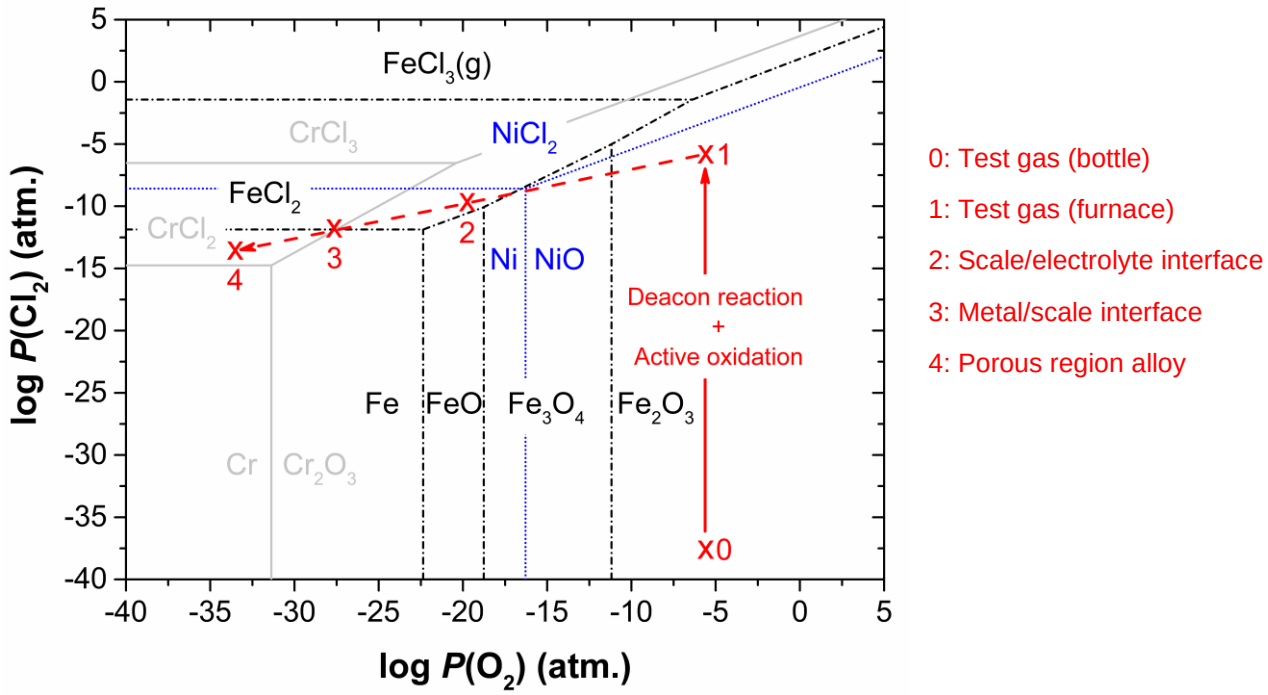

Fig. 14. Superimposed thermodynamic stability diagram of the Cr-Fe-Ni-Cl-O system at 700°C. The solid arrow from mark 0 to mark 1 illustrates the increase in Cl_2 partial pressure associated with the Deacon reaction (7) upon heating of the salt mixture and the active oxidation reactions (22)-(25). The semi-continuous arrow from marks 1 to 4 illustrates the evolution of the partial pressures of O_2 and Cl_2 from the gas phase towards the corroded region of the alloys upon exposure to the NaCl-KCl-$MgCl_2$ ternary mixture.

The production of O^{2-} in the melt will in turn change the local acidic/basic character of the melt and potentially lead to fluxing mechanisms of the oxide scales as predicted and validated electrochemically by Rapp and co-workers in molten sulfates [69,70]. As already mentioned, a low concentration of Fe was measured in the scales indicating that a significant fraction of $FeCl_2$ did not react with dissolved oxygen. Although gaseous $FeCl_2$ molecules may have been swept away by the Ar flow, it is also possible that a fraction of $FeCl_2$ remained in the salt and formed ternary compounds such as Rinneite (i.e. $3KCl.NaCl.FeCl_2$) after cooling of the samples as shown in [55] and in our previous study [34]. Fig. 4b is particularly interesting since Ni-rich particles, coming from Inconel 600 substrate, were embedded in MgO. First, this indicates that Ni is thermodynamically stable in the electrolyte and that the Cl_2 partial pressure does not exceed 10^{-8} atm. within the melt (see Fig. 14). This also suggests that these Ni-rich particles may have acted as cathodic sites to foster the reduction of $MgOH^+$ impurities following reaction (15). This hypothesis is in good agreement with the results of Ding et al. showing a deposited MgO-lump on a tungsten cathode after purifying a mixture of NaCl-KCl-$MgCl_2$ [30]. The estimated partial pressures of O_2 and Cl_2 in different locations of the samples are reported on Fig. 14 based on the experimental observations.

Whereas "chlorine-induced" corrosion mechanisms usually consider the direct reaction of Cl_2 molecules with metallic alloys [29,42,67] following adsorption and dissociation of the diatomic molecule, the formation of chloride compounds by ionic counter-migration is more likely to happen in molten chlorides since the Cl^- anion has a smaller size and higher mobility than Cl_2 [68]. In addition, the Deacon reaction (7) has a positive Gibbs free energy of formation at 700°C and is not spontaneous at the testing temperature. Nevertheless, this reaction is spontaneous at temperatures lower than 600°C and it is possible that it takes place in a different region of the furnace (colder parts of the furnace instead of the hot zone). These considerations may be of great interest for industrial CSP plants during night/day cycles since the molten salt storage tanks are alternatingly filled and emptied. One could expect chlorine-induced corrosion in regions not immersed in the salt (where the adsorption of Cl_2 molecules is favored), which could significantly impair the corrosion resistance of the structural materials.

4.3. Fluxing mechanisms and formation of $MgCr_2O_4$ spinel

Even though the formation of $MgCr_2O_4$ spinel has been reported nearly systematically during exposure of iron- and nickel-based superalloys in molten chlorides [7,16,19,23], its mechanisms of formation are not fully explained and we therefore propose to bridge the gap in this study. As mentioned in section 4.2, the formation of $MgCr_2O_4$ was intrinsically linked to the availability of O_2. For instance, the experimental observations indicate that the periphery of MgO crystals was in general converted into $MgCr_2O_4$ in the upper part of the salt (Fig. 4a and c) whereas such a conversion was marginally observed deep in the melt (Fig. 4b) where the amount of dissolved O_2 has to be lower because of diffusion limitations from the cover gas. Another important observation is that unlike in molten NaCl-KCl [34], Cr_2O_3 was not observed on all samples' surfaces and Cr was systematically present in the corrosion products as $MgCr_2O_4$ and in a small amount in MgO as confirmed by the fluorescence signals of Cr^{3+} cations in MgO obtained by Raman micro-spectrometry (Fig. 9). This therefore indicates that an interaction between MgO and Cr_2O_3 systematically occurred and was accelerated by O_2.

Since MgO is a basic oxide and Cr_2O_3 is a comparatively acidic oxide (according to Lux-Flood concept of acid/base reactions [69,70]), a synergistic dissolution of both oxides by exchange of O^{2-} is expected in molten salts following the works of Rapp and co-workers [71,72] (its occurrence depends on the local activity of O^{2-} anions). This coupling is therefore expected to accelerate simultaneously the acidic fluxing of MgO (28) and the basic fluxing of Cr_2O_3 (29) resulting in the formation of $MgCr_2O_4$ as a reaction product (30):

$MgO(s) \rightarrow Mg^{2+} + O^{2-}$ (acidic fluxing) (28)

$Cr_2O_3(s) + O^{2-} \rightarrow 2CrO_2^-$ (basic fluxing) (29)

$MgO(s) + Cr_2O_3(s) \rightarrow Mg^{2+} + 2CrO_2^- \rightarrow MgCr_2O_4(s)$ (synergistic dissolution) (30)

The relative basicity of NaCl-KCl-$MgCl_2$ ternary melt precludes the stability of Cr_2O_3 that systematically undergoes basic fluxing and transforms into $MgCr_2O_4$. However, the mechanisms must also take into consideration the initial nucleation of Cr_2O_3 on MgO to enable their synergistic dissolution. This may be because the nucleation of Cr_2O_3 is energetically favored on MgO serving as a support for reaction (22) in a region where the partial pressure of oxygen is sufficient to transform $CrCl_2$ into Cr_2O_3. A striking observation to support this hypothesis is the growth of thick $MgCr_2O_4$ scales on the Al_2O_3 rods used to hang the samples vertically in the melt (see Fig. 2a) in the form of very large crystals (Fig. 15). It is very likely that the corundum structure of the Al_2O_3 rods acted as nucleation site for Cr_2O_3, which also possesses the corundum structure. Since the rod was in a region with a higher availability of oxygen (a thin film of salt was most likely wetting the rod upon exposure as observed in Fig. 15a), the reaction of volatile $CrCl_2$ with O_2 was favored. The nucleation and growth of Cr_2O_3 on the Al_2O_3 template therefore occurred. Because the rod was in electrical contact with the alloy substrate and since Cr_2O_3 possesses semi-conducting properties at elevated temperatures [73], the reduction of $MgOH^+$ into MgO on Cr_2O_3 was kinetically favored. Then the simultaneous formation of MgO and Cr_2O_3 provoked the synergistic dissolution described in reaction (30) leading to the formation of $MgCr_2O_4$. These mechanisms are summarized in Fig. 16. It should be noted here that despite being an efficient electrical insulator, the formation of $MgCr_2O_4$ on Al_2O_3 poisoned its insulating behavior. A similar effect can therefore be expected within the MgO scales since their progressive conversion into $MgCr_2O_4$ occurred with increasing exposure time (compare Fig. 11a, c and e).

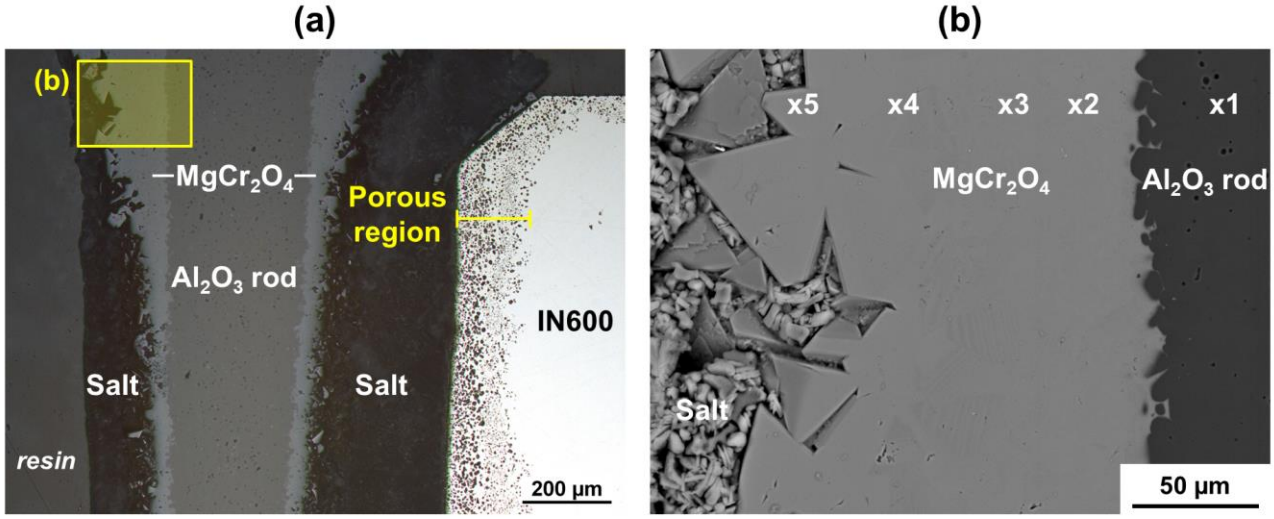

(c)

EDX spot	O	Al	Mg	Cr	Fe
1	58.0	42.0	-	-	-
2	61.3	-	16.7	21.3	0.7
3	61.8	-	16.0	21.6	0.6
4	61.9	-	16.4	21.0	0.6
5	63.1	-	15.5	21.0	0.4

Fig. 15. (a) Light optical cross-section image and (b) BSE-cross section image at higher magnification highlighting the formation of $MgCr_2O_4$ scales on the Al_2O_3 rod used to hang the samples vertically (see **Fig. 2**a). EDX spot measurements shown in (b) are summarized in the Table in (c) (at.%). The deviation of the magnesiochromite from the ideal $MgCr_2O_4$ stoichiometry probably explains its high electrical conductivity and its poisoning effect regarding the ohmic drop provided by MgO on the alloys' surfaces. For the sake of clarity, it was decided to note magnesiochromite as $MgCr_2O_4$ even though a more appropriate way of writing is $(Mg,Fe^{2+})_{1+x}(Cr,Fe^{3+})_{2-x}O_4$.

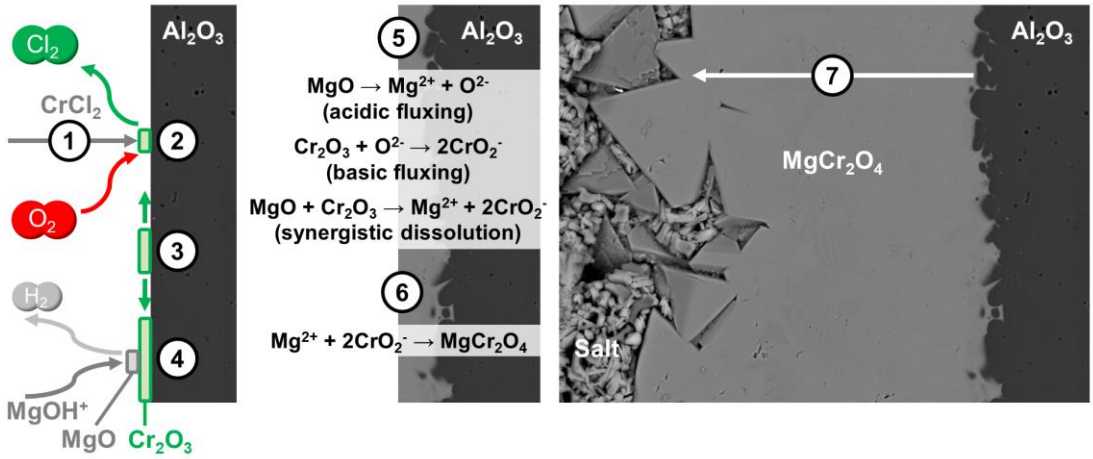

1- Formation of gaseous $CrCl_2$ at the metal/electrolyte interface and diffusion in the melt

2- Reaction of $CrCl_2$ with dissolved oxygen and nucleation of Cr_2O_3 on the Al_2O_3 template

3- Lateral growth of Cr_2O_3

4- $MgOH^+$ reduction into MgO kinetically favored on Cr_2O_3

5- Synergistic dissolution of MgO and Cr_2O_3 by fluxing mechanisms

6- Formation of $MgCr_2O_4$ as reaction product

7- Thickening of the $MgCr_2O_4$ scale by repetition of steps 1-6

Fig. 16. Proposed mechanisms of formation of magnesiochromite on Al_2O_3. The same mechanisms are expected to take place on growing MgO scales such that their periphery is always converted into $MgCr_2O_4$. Because the synergistic dissolution of MgO and Cr_2O_3 readily occurs, step 4 is only an intermediate of reaction (the interface MgO-Cr_2O_3 is metastable).

In fact, the higher corrosion rates on the outer region (Fig. 7a and b) than on the immersed region of the samples (Fig. 7c and d) suggest that the formation of $MgCr_2O_4$ at the expense of MgO decreases the corrosion resistance of the alloys. The detrimental influence of $MgCr_2O_4$ may be a consequence of its high electrical conductivity ($\sigma \approx 10^{-2}$ $\Omega^{-1}.cm^{-1}$ at 800°C [74]) in comparison to MgO ($\approx 10^{-11}$ $\Omega^{-1}.cm^{-1}$ at 700°C [66]). The formation of $MgCr_2O_4$ spinel would therefore inhibit the beneficial effect of MgO by increasing the charge-transfer rates between alloys and the electrolyte. Nevertheless, it should be mentioned that the presence of $MgCr_2O_4$ is alternatively a cause and a consequence of enhanced Cr dissolution from the substrate and that it is rather the availability of oxygen that plays a significant role in the overall corrosion mechanisms; (i) by reacting with gaseous metal chlorides releasing chlorine and (ii) by feeding the cathodic reaction.

4.4. Compositional and microstructural effects

The driving force for electrochemical corrosion is further increased with a larger difference of potentials between cathodic and anodic areas, an increased mobility of charges in the electrolyte and in the metal and a larger cathode/anode surface ratio. In the particular case of molten chlorides, the corrosion of metallic alloys is mainly attributed to the selective dissolution of Cr [7,8,20,21,34]. Therefore, compositional and microstructural features of the alloys, especially its Cr distribution, will greatly influence their corrosion behavior in molten chlorides. Since the corrosion experiments were carried out at 700°C, solid-state diffusion mechanisms within the alloys must be taken into account to further understand the corrosion mechanisms. The microstructural instability of metallic alloys was indeed reckoned to influence the propagation of the corrosion in molten chlorides [34,64,65] as well as in chloride-carbonate mixtures [45]. Bell et al. concluded that the vulnerability of nickel-based alloy 601 resulted from the dissolution of carbide forming elements Cr and Mn [45]. However, the same authors indicated that it is

unclear if the carbide phases are being removed or if there is a link between the carbide formation and their proneness for dissolution.

In this study, metal loss measurements and metallographic observations clearly indicate that the ferritic-martensitic P91 steel is more resistant than Inconel 600 when exposed to molten NaCl-KCl-$MgCl_2$ at 700°C. As revealed by electrochemical etching in Fig. 1a and elsewhere [35,36], the tempered ferritic-martensitic microstructure of P91 shows carbides (mostly Cr-rich $M_{23}C_6$ carbides) at the prior austenite grain boundaries and between lath boundaries. While BSE cross-section images of P91 after exposure unambiguously revealed the selective removal of these Cr-rich carbides leaving voids mostly at the prior austenite grain boundaries after 100 and 300 h exposure (Fig. 8c-f), the Fe-rich metallic matrix also suffered corrosion in the early stage of exposure (Fig. 8a-b and Fig. 10). The systematic presence of Mo-rich particles within MgO scales (Fig. 10a-c), most likely corresponding to Mo-rich laves phases [75] although further characterization techniques (e.g. TEM) should be employed, may indicate that they supported the cathodic reaction (reduction of corrosive $MgOH^+$ species). This is a very important finding, since several studies use Mo crucibles for molten chloride exposures. With a small cathode/anode surface ratio, the driving force for corrosion of P91 steel is relatively low, which could explain its comparably good behavior in molten NaCl-KCl-$MgCl_2$ at 700°C. This results in the formation of relatively pure MgO scales on the surface of P91 although $MgCr_2O_4$ spinel, indicating the outward transport of Cr species from the alloy to the scales, is also observed. P91 steel also has a lower nominal concentration of Cr than Inconel 600 (see Table 1), which may also contribute to the fact that less Cr was available to form $MgCr_2O_4$ spinel on P91 surfaces.

As commonly reported in the literature [76,77], Cr-rich $M_{23}C_6$ and M_7C_3 carbides are confined at the grain boundaries in the pristine solution-annealed microstructure of Inconel 600 (Fig. 1b). However, heat treating Inconel 600 in the vicinity of 700°C will foster the precipitation of intragranular Cr-rich carbides within the γ-(Ni) solid solution matrix and limit sensitization of the grain boundaries [76,77,78]. This was indeed observed in Fig. 12c and d with both intergranular and intragranular carbides below the corrosion front. In molten NaCl-KCl-$MgCl_2$, the electromotive forces are in the order $Cr^{2+}/Cr < Fe^{2+}/Fe < Ni^{2+}/Ni$ [31]. Consequently, the difference in potentials between the Cr-rich phases (e.g. Cr-rich $M_{23}C_6$ or M_7C_3 carbides) and Ni-rich matrix results in the formation of electrochemical cells. With a lower electrode potential, Cr is then selectively dissolved from the alloy leaving voids within the microstructure (see Fig. 11). This hypothesis is in good agreement with the experimental observations of Abramov and co-workers [64,65] as well as with our previous study [34] indicating the formation of micro-galvanic pairs between the γ-(Ni) solid solution matrix and secondary phases when exposing nickel-based alloys to molten chlorides. The driving force of the corrosion attack is further increased by the large cathode/anode surface ratio. As a result, Cr-rich carbides are continuously dissolved as the electrolyte permeates through the porous oxide scales and the porous region of the substrate by capillary effects as proposed by Bell et al. [45]. The outward transport of Cr as gaseous $CrCl_2$ and its reaction with oxygen above the surface of the alloy results in the formation of magnesiochromite as discussed in sections 4.2 and 4.3. The continuous dissolution of Cr progressively enriches the corrosion scales in magnesiochromite, especially in the outer region of the samples where there is a higher O_2 availability (compare Fig. 12a and b). As aforementioned, $MgCr_2O_4$ has a higher electrical conductivity ($\sigma \approx 10^{-2}\ \Omega^{-1}.cm^{-1}$ at 800°C [74]) than MgO ($\approx 10^{-11}\ \Omega^{-1}.cm^{-1}$ at 700°C [66]), which increases the charge-transfer reaction rates. The enrichment of the scales in $MgCr_2O_4$ at the expense of MgO results in a positive feedback loop regarding further corrosion attack of Inconel 600. This effect is likely to explain the higher corrosion rates noted on the outer region than on the immersed region of the samples (compare Fig. 7b and d).

It should be noticed that similar microstructural observations were given after exposure of iron- and nickel-based alloys in Cl_2-contanining environments with a porous "sponge-like" microstructure of the alloys' subsurface region and chains of pores along the grain boundaries [42,67]. Grabke et al. indicated that the carbides were preferentially attacked by Cl_2 leaving holes in the metal matrix through the formation of gaseous metal chlorides following reaction (31) in the case of $Cr_{23}C_6$ carbides [42]:

$$Cr_{23}C_6(s) + 23Cl_2(g) + 3O_2(g) \rightleftarrows 23CrCl_2(s,g) + 6CO(g) \qquad (\Delta_rG°_{700°C} = -4985.6\ kJ) \qquad (31)$$

Similarly, Bender and Schütze proposed reaction (32) for the preferential attack of Cr_7C_3 carbides releasing gaseous CO_2 and volatile chloride compounds [67]:

$$Cr_7C_3(s) + 7Cl_2(g) + 3O_2(g) \rightleftarrows 7CrCl_2(s,g) + 3CO_2(g) \qquad (\Delta_rG°_{700°C} = -2286.7\ kJ) \qquad (32)$$

Considering the low oxygen partial pressure ($< 10^{-32}$ atm.) prevailing at the reaction front in the melt in the present study (see Fig. 12c and d for an illustration), the formation of gaseous CO and CO_2 is not thermodynamically favored with equilibrium oxygen partial pressures of about $3.1x10^{-22}$ and $5.5x10^{-22}$ atm. at 700°C, respectively. In addition, considerations in section 4.1 suggest that the attack is dominated by electrochemical corrosion rather than chlorine-induced corrosion. Despite negative Gibbs free energies, reactions (31) and (32) cannot take place within the alloy and the general reaction associated with carbide dissolution can therefore be written:

$$Cr_xC_y + 2xCl^- \rightleftarrows xCrCl_2(s,g) + 2xe^- + yC(s) \qquad (33)$$

where Cr_xC_y corresponds to Cr-rich carbides (e.g. Cr_7C_3 or $Cr_{23}C_6$).

Reaction (33) can therefore be interpreted as the partial anodic reaction. Because carbon is stable at such low oxygen partial pressures, it diffuses back to the γ-(Ni) solid solution matrix. Since carbon has a low solubility in γ-(Ni) and its diffusivity in Ni ($\approx 10^{-9}$ cm^2/s at 700°C [79]) is larger than the diffusivity of Cr in Ni ($\approx 10^{-11}$ cm^2/s at 700°C [80]), further precipitation of Cr-rich carbides occurs within the alloy matrix, as observed in Fig. 12c and d and in Refs. [34,45]. This results in a self-sustaining attack driven by solid-state diffusion mechanisms within the alloy following alternative precipitation/dissolution of Cr-rich carbides and formation of void channels. In addition, this will drastically decrease the mechanical strength of solution-strengthened alloys such as Inconel 600 in which carbide precipitation increases the tensile strength and creep resistance. While the formation of void channels is mainly assigned to the selective dissolution of Cr-rich carbides, it is likely that the defective structure of the alloy in the vicinity of the carbides is also prone to dissolution and the accumulation of defects such as vacancies may further aggravate the formation of a porous microstructure. Fine-scale characterization (e.g. TEM) should be conducted to verify the validity of these hypotheses. Nevertheless, our findings clearly demonstrate that considering a nickel-based alloy to be, *de facto*, more corrosion resistant than any given steel in chloride melts might not be necessarily true and that microstructural instability (e.g. distribution of Cr-rich phases, diffusion flux of Cr from the alloy, C solubility and mobility) may shorten the lifetime of an otherwise stable metallic matrix. These insights should also be put in perspective with mechanical considerations and thermal cycling conditions that will also influence the overall lifetime of the components.

4.5. Influence of testing conditions on the experimental corrosion rates: focus on $MgCl_2$

The metal loss data presented in Fig. 6 clearly indicates that the corrosion attack of P91 and Inconel 600 is more pronounced in the binary NaCl-KCl compared to the ternary NaCl-KCl-$MgCl_2$ melt. For instance, the empirical median corrosion rate calculated from the metal loss data is about 30 times greater for Inconel 600 immersed in molten NaCl-KCl (7194 µm/year [34]) than in molten NaCl-KCl-$MgCl_2$ (212 µm/year, Fig. 7d). Similar observations are made after exposure of P91 in molten NaCl-KCl-$MgCl_2$ with median corrosion rates about 6 to 30 times smaller than after exposure to the binary NaCl-KCl salt mixture. In addition, whereas P91 is sensitive to pitting corrosion in molten NaCl-KCl, as presented in our previous study [34], the presence of $MgCl_2$ within the melt inhibits this phenomenon due to the formation of MgO. This considerably affected the maximum corrosion rates recorded on P91 locally exceeding 10 mm/year in NaCl-KCl melt to only about 200 µm/year in the ternary salt mixture.

At first view, these results seem to be in contradiction with the findings of Zhu et al. in Ref. [81]. In their work, the authors investigated the corrosion behavior of Inconel 625 in molten NaCl, KCl, $CaCl_2$ and $MgCl_2$ as well as in different chloride mixtures (e.g. NaCl-$MgCl_2$, KCl-$MgCl_2$, NaCl-$CaCl_2$ and KCl-$CaCl_2$). After 20 h of exposure at 900°C, Inconel 625 was found to suffer more severe corrosion in molten $MgCl_2$ and in molten chloride mixtures with high $MgCl_2$ contents. The authors attributed this to the higher hygroscopicity of $MgCl_2$ resulting in a higher basicity (i.e. higher activity of O^{2-} anions) of the melt [81]. In fact, the higher the basicity of the melt, the easier the dissolution of Cr_2O_3 into chromate anions (CrO_4^{2-}) following basic fluxing mechanisms [72]. In addition, Zhu et al. carried out the experiments in air, which further increased the basicity of the molten salts. It should also be pointed out that while the authors used anhydrous NaCl and KCl salts, $MgCl_2$ was hydrous resulting in a very high level of corrosive $MgOH^+$ impurities within the melt after heating (see the reaction pathways (1)-(5)). These testing conditions intensified the negative influence of $MgCl_2$ on the corrosion behavior of Inconel 625 at 900°C [81]. Overall, the salt mixtures with $MgCl_2$ were then more corrosive than the ones without $MgCl_2$.

Unlike Zhu et al. [81], our experiments were carried out at 700°C in Ar and with anhydrous $MgCl_2$ (although partially hydrated by the initial weighing and the transfer of the samples to the reaction chamber). In such testing conditions, the activity of O^{2-} anions is expected to be much lower such that the basic fluxing of Cr_2O_3 does not form chromate but chromite anions as discussed in section 4.3. Moreover, the use of anhydrous $MgCl_2$ considerably limited the introduction of water molecules in the furnace and the consequential hydrolysis reactions (see the reaction pathways (1)-(5)). This resulted in a lower concentration of corrosive $MgOH^+$ impurities after heating of the salt mixture and thus led to a lower extent of metal dissolution as presented in Fig. 13. As discussed in section 4.1, the reduction of $MgOH^+$ on the metallic substrates forms relatively continuous MgO scales presenting a low solubility in the melt. Once the concentration of $MgOH^+$ impurities reaches negligible amounts, these MgO scales form a physical barrier against further diffusion of other oxidants such as O_2. With a low electrical conductivity, MgO decreases the intensity of the cathodic reactions and, as a result, slows down the metal dissolution rate. In fact, the most important degradation mechanism of such MgO scales was caused by their synergistic dissolution with Cr_2O_3 forming $MgCr_2O_4$ spinel characterized by a significantly higher electrical conductivity than MgO.

To conclude, it appears that depending on the testing conditions (e.g. gas composition, temperature, use of hydrous or anhydrous salts), $MgCl_2$ can be classified as detrimental or relatively beneficial in comparison to molten chlorides not containing $MgCl_2$ when considering the corrosion behavior of structural materials. The fact that the experimental testing conditions can lead to different conclusions while investigating the effect of a single parameter should be regarded as of the utmost importance. The development of new standard test methods for molten salt corrosion, especially when handling hygroscopic salts such as $MgCl_2$, should therefore be considered

to design corrosion experiments at laboratory scale. This would provide significant insight into corrosion issues under in-service conditions, which is critical for successful plant design.

5. Conclusions

The corrosion behavior of ferritic-martensitic P91 steel and Inconel 600 nickel-based alloy in molten NaCl-KCl-$MgCl_2$ (24.5-20.5-55.0 wt.%) has been investigated at 700°C under Ar. Based on the experimental observations, the following conclusions can be drawn:

(1) Both alloys showed impurity-driven corrosion mechanisms associated with the formation of corrosive $MgOH^+$ impurities within the melt upon thermal hydrolysis of $MgCl_2$. This electrochemical process combines the reduction of $MgOH^+$ into insoluble MgO on the surface and metal dissolution from the substrates. The precipitation of MgO at the metal/electrolyte interface resulted in a relatively protective behavior under isothermal and static conditions, especially for P91 steel.

(2) The corrosion attack was associated with the selective dissolution of Cr and the removal of Cr-rich carbides from the alloy matrix. The microstructural instability of Inconel 600 at 700°C with excessive formation of intragranular Cr-rich carbides within the γ-(Ni) solid solution matrix led to the formation of galvanic pairs. The alternative precipitation and dissolution of Cr-rich carbides resulted in the formation of chains of pores within the alloy, which was further aggravated by solid-state diffusion mechanisms.

(3) The O_2 availability had a clear effect on the corrosion kinetics by shifting the equilibrium reactions towards oxidation of gaseous $CrCl_2$ species into Cr_2O_3 as well as by participating in the cathodic activity once the concentration of $MgOH^+$ impurities reached negligible levels.

(4) The ferritic-martensitic P91 steel showed a better corrosion resistance than Inconel 600 in molten NaCl-KCl-$MgCl_2$. This was attributed to a lower potential difference between Cr-rich phases and the Fe-rich matrix than between Cr-rich phases and the Ni-rich matrix, respectively. In addition, the higher dissolution rate of Cr and outward transport of Cr-containing species in the case of Inconel 600 resulted in a larger fraction of $MgCr_2O_4$ spinel at the expense of MgO within the corrosion products.

(5) The mechanisms of formation of $MgCr_2O_4$ spinel, commonly observed within the corrosion products of iron- and nickel-based materials immersed in molten chlorides, were elucidated. These mechanisms involve the synergistic dissolution of MgO and Cr_2O_3 forming $MgCr_2O_4$ as reaction product of the acidic fluxing of MgO ($MgO \rightarrow Mg^{2+} + O^{2-}$) and basic fluxing of Cr_2O_3 ($Cr_2O_3 + O^{2-} \rightarrow 2CrO_2^-$). This resulted in the conversion of MgO into $MgCr_2O_4$ over time, which poisoned the electrical insulation capacity of MgO due to the higher electrical conductivity of $MgCr_2O_4$ spinel compared to MgO.

Acknowledgements

The European Union's Horizon 2020 research and innovation program is gratefully acknowledged for funding this research (RAISELIFE, grant agreement No. 686008). The authors would like to thank Daniela Hasenpflug and Ellen Berghof-Hasselbächer for helping with the metallographic preparation of the samples. Susann Rudolphi is gratefully acknowledged for performing the optical emission spectrometry (OES) measurements of the alloys.

Appendix

The fluorescence of Cr^{3+} ions in MgO has long been used to characterize the MgO cubic structure with a sharp emission line (R-line) centered at 698.1 nm at 77 K in a purely cubic field [58,82,83,84]. In 1932, Deutschbein has shown that additional vibrational bands are associated to the fluorescence of Cr^{3+} ions in MgO and gave their corresponding emission wavelengths and width in frequency (cm^{-1}) at both 20°C and -195°C [58]. The ionoluminescence of the MgO:Cr^{3+} system is very sensitive even at very low concentration of Cr^{3+}, e.g. below the detection limit of ICP-OES (inductively coupled plasma optical emission spectrometry) and in the detection limit of PIXE (proton-induced X-ray emission) [85]. With the appropriate laser source, Raman spectroscopy therefore appears very promising to characterize the physical properties of MgO by Cr^{3+} fluorescence. The Raman shift values associated with the fluorescence bands of the MgO:Cr^{3+} system were calculated from the emission wavelengths given in the work of Deutschbein (see Table 2) for both Nd:YAG (λ_{exc} = 532.0 nm) and He-Ne (λ_{exc} = 632.8 nm) lasers following equation (30):

$$\Delta\omega = \left(\frac{10^7}{\lambda_{exc}} - \frac{10^7}{\lambda_{emission}}\right) \quad (30)$$

where λ_{exc} corresponds to the wavelength of the laser source in nm, $\lambda_{emission}$ corresponds to the emission wavelength of the fluorescence band in nm and $\Delta\omega$ its corresponding Raman shift in cm^{-1}.

Table 2
Summary of the fluorescence emission bands identified in the MgO:Cr^{3+} system at 20°C by Deutschbein [58] and their corresponding Raman shift values calculated for the Nd:YAG (λ_{exc} = 532.0 nm) and He-Ne (λ_{exc} = 632.8 nm) lasers. The experimental data obtained in this study for a reference MgO powder (see Fig. 17) are given in the last two columns and fairly agree with the theoretical calculations.

Fluorescence emission bands				Raman shift values (cm^{-1})			
Band	$\lambda_{emission}$ (nm)	Relative intensity	Width (cm^{-1})	Calculated from [58]		This study (MgO powder)	
				λ_{exc} = 532.0 nm	λ_{exc} = 632.8 nm	λ_{exc} = 532.0 nm	λ_{exc} = 632.8 nm
γ_b	673.9	2	40	3958	964	3958	969
β_b	679.3	4	60	4076	1082	4078	1098
α_b	686.7	2	50	4235	1240	4239	1257
R	699.1	10	12	4493	1499	4485	1499
N	704.7	7	15	4607	1612	-	-
α_r	712.6	2	50	4764	1770	4750	1770
β_r	720.5	4	130	4918	1924	4914	1932
γ_r	726.9	2	40	5040	2046	5015	2033
$2\beta_r$	743.3	2	120	5343	2349	5321	2349

The experimental Raman shift values associated with the fluorescence bands of Cr^{3+} in the reference MgO powder are in good agreement with the theoretical calculations for both laser sources (see Table 2). These fluorescence bands were labelled accordingly in Fig. 9 and Fig. 17. Unlike the spectra obtained for the MgO scales in Fig. 9, the N-line corresponding to the electric dipole of locally compensated Cr^{3+} tetragonal centers [84] was not observed for the reference MgO powder (Fig. 17a and b). Since there is a dependence of the N-line intensity on the Cr^{3+} concentration in MgO [83], this may indicate different levels of Cr impurities within the MgO crystals. The Cr^{3+} concentration is indeed expected to be higher in the MgO scales formed during the molten salt exposures than in the reference MgO powder (< 5 ppm according to the furnisher).

Whereas three additional Raman bands centered at 275, 441 and 1076 cm^{-1} are observed in Fig. 17a, only one Raman mode centered at 441 cm^{-1} is observed in Fig. 17b. The fact that the other two Raman modes (275 and 1076 cm^{-1}) were not observed with the He-Ne laser may be related to the higher fluorescence background, which probably masked the low intensity vibrational modes in the Raman range. The two bands centered at 275 and 441 cm^{-1} correspond to MgO [86]. To the best of the authors' knowledge, the additional Raman mode at 1076 cm^{-1} does not correspond with a known Raman active mode of MgO. Since magnesium carbonate is the main impurity in the MgO powder (≤ 1.5% according to the furnisher), this vibrational mode may be attributed to the C-O symmetry-stretch of magnesite (i.e. $MgCO_3$) following the work of Jiang et al. [87]. The presence of $MgCO_3$ residues in the MgO powder may have resulted from an incomplete calcination process since MgO powder is obtained by calcination of magnesite in air [88].

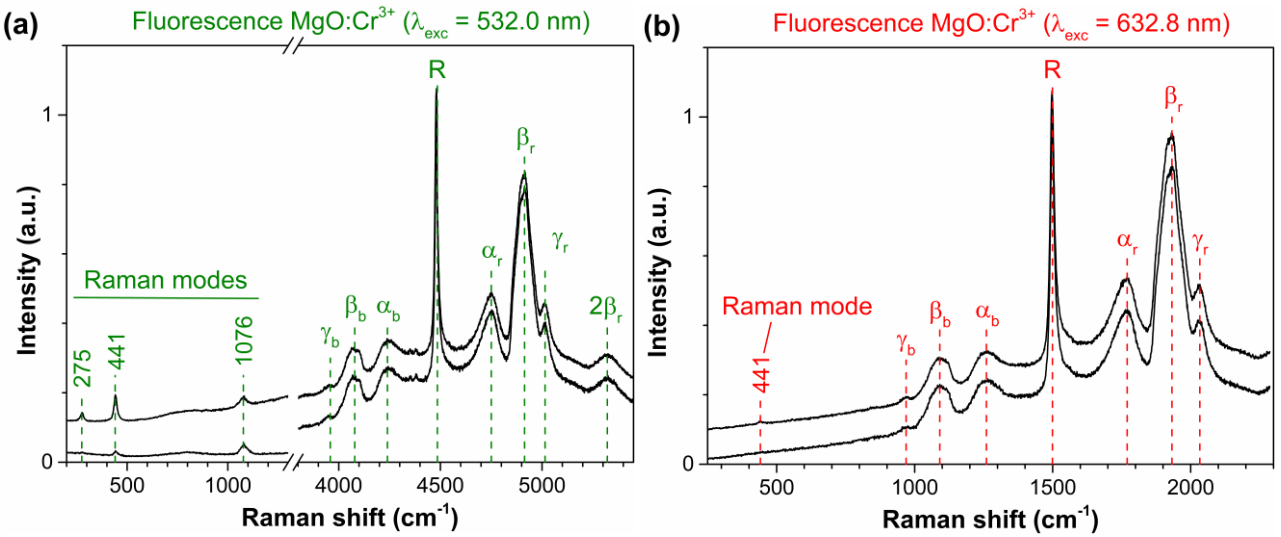

Fig. 17. Raman and fluorescence bands obtained with (a) Nd:YAG laser (λ_{exc} = 532.0 nm) and (b) He-Ne laser (λ_{exc} = 632.8 nm) for a reference MgO powder. Please note the *x*-axis break in Fig. 17a.

References

[1] D.A. Baharoon, H.A. Rahman, W.Z. Wan Omar, S.O. Fadhl, Historical development of concentrating solar power technologies to generate clean electricity efficiently – A review, *Renew. Sustain. Energy Rev. 41* (2015) 996-1027.

[2] Md Tasbirul Islam, N. Huda, A.B. Abdullah, R. Saidur, A comprehensive review of state-of-the-art concentrating solar power (CSP) technologies: Current status and research trends, *Renew. Sustain. Energy Rev. 91* (2018) 987-1018.

[3] M. Sarvghad, S. Delkasar Maher, D. Collard, M. Tassan, G. Will, T.A. Steinberg, Materials compatibility for the next generation of concentrated solar power plants, *Energy Storage Mater. 14* (2018) 179-198.

[4] K. Vignarooban, X. Xu, A. Arvay, K. Hsu, A.M. Kannan, Heat transfer fluids for concentrating solar power systems – A review, *Appl. Energy 146* (2015) 383-396.

[5] J.I. Burgaleta, S. Arias, D. Ramirez, Gemasolar, the first tower thermosolar commercial plant with molten salt storage, *Proceedings of the SolarPACES 2011 conference on concentrating solar power and chemical energy systems*, Granada, Spain. 2011.

[6] A. Bonk, S. Sau, N. Uranga, M. Hernaiz, T. Bauer, Advanced heat transfer fluids for direct molten salt line-focusing CSP plants, *Prog. Energy Combust. Sci. 67* (2018) 69-87.

[7] W. Ding, H. Shi, Y. Xiu, A. Bonk, A. Weisenburger, A. Jianu, T. Bauer, Hot corrosion behavior of commercial alloys in thermal energy storage material of molten $MgCl_2$/KCl/NaCl under inert atmosphere, *Sol. Energy Mater. Sol. Cells 184* (2018) 22-30.

[8] W. Ding, H. Shi, A. Jianu, Y. Xiu, A. Bonk, A. Weisenburger, T. Bauer, Molten chloride salts for next generation concentrated solar power plants: Mitigation strategies against corrosion of structural materials, *Sol. Energy Mater. Sol. Cells 193* (2019) 298-313.

[9] A. Bonk, D. Rückle, S.Kaesche, M. Braun, T. Bauer, Impact of solar salt aging on corrosion of martensitic and austenitic steel for concentrating solar power plants, *Sol. Energy Mater. Sol. Cells 203* (2020) 110162.

[10] Y. Li, X. Xu, X. Wang, P. Li, Q. Hao, B. Xiao, Survey and evaluation of equations for thermophysical properties of binary/ternary eutectic salts from NaCl, KCl, $MgCl_2$, $CaCl_2$, $ZnCl_2$ for heat transfer and thermal storage fluids in CSP, *Sol. Energy 152* (2017) 57-79.

[11] X. Xu, G. Dehghani, J. Ning, P. Li, Basic properties of eutectic chloride salts NaCl-KCl-$ZnCl_2$ and NaCl-KCl-$MgCl_2$ as HTFs and thermal storage media measured using simultaneous DSC-TGA, *Sol. Energy 162* (2018) 431-441.

[12] G. Mohan, M. Venkataraman, J. Gomez-Vidal, J. Coventry, Thermo-economic analysis of high-temperature sensible thermal energy storage with different ternary eutectic alkali and alkaline earth metal chlorides, *Sol. Energy 176* (2018) 350-357.

[13] G. Alva, L. Liu, X. Huang, G. Fang, Thermal energy storage materials and systems for solar energy applications, *Renew. Sustain. Energy Rev. 68* (2017) 693-706.

[14] P.D. Myers Jr., D. Yogi Goswami, Thermal Energy storage using chloride salts and their eutectics, *Appl. Therm. Eng. 109* (2016) 889-900.

[15] G. Mohan, M. Venkataraman, J. Gomez-Vidal, J. Coventry, Assessment of a novel ternary eutectic chloride salt for next generation high-temperature sensible heat storage, *Energy Convers. Manag. 167* (2018) 156-164.

[16] A.G. Fernández, L.F. Cabeza, Corrosion evaluation of eutectic chloride molten salt for new generation of CSP plants. Part I: Thermal treatment assessment, *J. Energy Storage 27* (2020) 101125.

[17] A.M. Kruizenga, Corrosion mechanisms in chloride and carbonate salts, Sandia Report No. SAND2012-7594, Sandia National Laboratories (2012).

[18] K. Vignarooban, X. Xu, K. Wang, E.E. Molina, P. Li, D. Gervasio, A.M. Kannan, Vapor pressure and corrosivity of ternary metal-chloride molten-salt based heat transfer fluids for use in concentrating solar power systems, *Appl. Energy 159* (2015) 206-213.

[19] B. Liu, X. Wei, W. Wang, J. Lu, J. Ding, Corrosion behavior of Ni-based alloys in molten NaCl-$CaCl_2$-$MgCl_2$ eutectic salt for concentrating solar power, *Sol. Energy Mater. Sol. Cells 170* (2017) 77-86.

[20] H. Sun, J. Wang, Z. Li, P. Zhang, X. Su, Corrosion behavior of 316SS and Ni-based alloys in a ternary NaCl-KCl-$MgCl_2$ molten salt, *Sol. Energy 171* (2018) 320-329.

[21] H. Sun, P. Zhang, J. Wang, Effect of alloying elements on the corrosion behavior of Ni-based alloys in molten NaCl-KCl-$MgCl_2$ salt at different temperatures, *Corr. Sci. 143* (2018) 187-199.

[22] J.C. Gomez-Vidal, A.G. Fernandez, R. Tirawat, C. Turchi, W. Huddleston, Corrosion resistance of alumina-forming alloys against molten chlorides for energy production. I: Pre-oxidation treatment and isothermal corrosion tests, *Sol. Energy Mater. Sol. Cells 166* (2017) 222-233.

[23] J.C. Gomez-Vidal, A.G. Fernandez, R. Tirawat, C. Turchi, W. Huddleston, Corrosion resistance of alumina-forming alloys against molten chlorides for energy production. II: Electrochemical impedance spectroscopy under thermal cycling conditions, *Sol. Energy Mater. Sol. Cells 166* (2017) 234-245.

[24] I.N. Ozeryanaya, Corrosion of metals by molten salts in heat-treatment processes, UDC 620.193.423, Plenum Publishing Corporation (1985) 184-188.

[25] S. Guo, J. Zhang, W. Wu, W. Zhou, Corrosion in the molten fluoride and chloride salts and materials development for nuclear applications, *Prog. Mater. Sci. 97* (2018) 448-487.

[26] J.C. Vidal, N. Klammer, Molten chloride technology pathway to meet the U.S. DOE SunShot initiative with Gen3 CSP, AIP Conference Proceedings 2126, 080006 (2019).

[27] S. Shoval, S. Yariv, Y. Kirsch, H. Peled, The effect of alkali halides on the thermal hydrolysis of magnesium chloride and magnesium bromide, *Thermochim. Acta 109* (1986) 207-226.

[28] H.E. Friedrich, B.L. Mordike, Magnesium technology. Metallurgy, Design data, Applications. ISBN-10 3-540-20599-3 Springer Berlin Heidelberg New York (2006).

[29] A. Zahs, M. Spiegel, J. Grabke, Chloridation and oxidation of iron, chromium, nickel and their alloys in chloridizing and oxidizing atmospheres at 400-700°C, *Corr. Sci. 42* (2000) 1093-1122.

[30] W. Ding, J. Gomez-Vidal, A. Bonk, T. Bauer, Molten chloride salts for next generation CSP plants: Electrolytical salt purification for reducing corrosive impurity level, *Sol. Energy Mater. Sol. Cells 199* (2019) 8-15.

[31] H.C. Gaur, H.L. Jindal, Standard electrode potentials in molten chlorides, *Electrochem. Acta 13* (1968) 835-842.

[32] D.D. Wagman, W.H. Evans, V.B. Parker, I. Halow, S.M. Bailey, R.H. Schumm, Selected values of chemical thermodynamic properties, National Bureau of Standards (1965).

[33] Y. Zhao, N. Klammer, J. Vidal, Purification strategy and effect of impurities on corrosivity of dehydrated carnallite for thermal solar applications, *RSC Adv. 9* (2019) 41664-41671.

[34] B. Grégoire, C. Oskay, T.M. Meißner, M.C. Galetz, Corrosion mechanisms of ferritic-martensitic P91 steel and Inconel 600 nickel-based alloy in molten chlorides. Part I: NaCl-KCl binary system, Accepted for publication in Sol. Energy Mater. Sol. Cells (2020).

[35] C. Pandey, A. Giri, M.M. Mahapatra, Evolution of phases in P91 steel in various heat treatment conditions and their effect on microstructure stability and mechanical properties, *Mater. Sci. Eng. A 664* (2016) 58-74.

[36] X. Zhang, Y. Zeng, W. Cai, Z. Wang, W. Li, Study on the softening mechanism of P91 steel, *Mater. Sci. Eng. A 728* (2018) 63-71.

[37] V. Encinas-Sánchez, M.T. de Miguel, M.I. Lasanta, G. García-Martín, F.J. Pérez, Electrochemical impedance spectroscopy (EIS): An efficient technique for monitoring corrosion processes in molten salt environments in CSP applications, *Sol. Energy. Mater. Sol. Cells 191* (2019) 157-163.

[38] C. Oskay, T.M. Meißner, C. Dobler, B. Grégoire, M.C. Galetz, Scale formation and degradation of diffusion coatings deposited on 9% Cr steel in molten solar salt, *Coatings 9* (2019) 687.

[39] H.Y. Zhang, Y.H. Lu, M. Ma, J. Li, Effect of precipitated carbides on the fretting wear behavior of Inconel 600 alloy, *Wear 315* (2014) 58-67.

[40] P.M. Scott, P. Combrade, General corrosion and stress corrosion cracking of Alloy 600 in light water reactor primary coolants, *J. Nucl. Mater. 524* (2019) 340-375.

[41] X. Zheng, R.A. Rapp, Chloridation-oxidation of nine commercial high-temperature alloys at 800°C, *Oxid. Met. 48* (1997) 553-596.

[42] H.J. Grabke, M. Spiegel, A. Zahs, Role of alloying elements and carbides in the chlorine-induced corrosion of steels and alloys, *Mater. Res. 7* (2004) 89-95.

[43] International Standard ISO, Corrosion of Metals and Alloys – Test Method for High Temperature Corrosion Testing of Metallic Materials by Immersing in Molten Salt or Other Liquids Under Static Conditions,17245 (2015).

[44] M. Sarvghad, G. Will, T.A. Steinberg, Corrosion of Inconel 601 in molten salts for thermal energy storage, *Sol. Energy Mater. Sol. Cells 172* (2017) 220-229.

[45] S. Bell, K. Lippiatt, T. Steinberg, G. Will, Damage analysis of 601 nickel superalloy in eutectic Na_2CO_3/NaCl molten salt under isothermal and thermal cycling conditions, *Sol. Energy 191* (2019) 637-646.

[46] W. Ding, A. Bonk, J. Gussone, T. Bauer, Cyclic voltammetry for monitoring corrosive impurities in molten chlorides for thermal energy storage, *Energy Procedia 135* (2017) 82-91.

[47] K. Rahts, M. Schorr, C. Schwaln, M. Schütze, Water-free methods of preparation for the analyses of chlorides in the high temperature oxidation in chloride containing atmospheres, *Prakt. Metallogr. 36* (1999) 86-97.

[48] M. Walczak, F. Pineda, A.G. Fernandez, C. Mata-Torres, R.A. Escobar, Materials corrosion for thermal energy storage systems in concentrated solar power plants, *Renew. Sustain. Energy Rev. 86* (2018) 22-44.

[49] S. Bell, T. Steinberg, G. Will, Corrosion mechanisms in molten salt thermal energy storage for concentrating solar power, *Renew. Sustain. Energy Rev. 114* (2019) 109238.

[50] International Standard ISO, Corrosion of Metals and Alloys – Method for Metallographic Examination of Samples After Exposure to High-temperature Corrosive Environments, 26146 (2012).

[51] J.R. Nicholls, N.J. Simms, A. Encinas-Oropesa, Modelling hot corrosion in industrial gas turbines, *Mater. High Temp. 24* (2007) 149-162.

[52] J. Sumner, A. Encinas-Oropesa, N.J. Simms, J.R. Nicholls, Type II hot corrosion: Behavior of CMSX-4 and IN738LC as a function of corrosion environment, *Mater. Corr. 65* (2014) 188-196.

[53] B. Grégoire, X. Montero, M.C. Galetz, G. Bonnet, F. Pedraza, Correlations between the kinetics and the mechanisms of hot corrosion of pure nickel at 700°C, *Corr. Sci. 155* (2019) 134-145.

[54] D.M. Smith, M.P. Neu, E. Garcia, L.A. Morales, Hydration of plutonium oxide and process salts, NaCl, KCl, $CaCl_2$, $MgCl_2$: effect of calcination on residual water and rehydration, *Waste Manag. 20* (2000) 479-490.

[55] H. Fink, H.J. Seifert, Quaternary compounds in the system NaCl-KCl-$MgCl_2$, *Thermochim. Acta 72* (1984) 195-200.

[56] R.E. Melchers, Predicting long-term corrosion of metal alloys in physical infrastructure, *NPJ Mater. Degrad. 4* (2019) 1-7.

[57] K. Sridharan, T.R. Allen, Molten salts chemistry. Chapter 12 – Corrosion in molten salts (2013) 241-267.

[58] O. Deutschbein, Die lienenhafte emission und absorption der chromosphore, *Annalen der Physik 406*, Issue 6 (1932) 712-728.

[59] Z. Wang, H.S.C. O'Neill, P. Lazor, S.K. Saxena, High pressure Raman spectroscopic study of spinel $MgCr_2O_4$, *J. Phys. Chem. Solids 63* (2002) 2057-2061.

[60] V. D'Ippolito, G.B. Andreozzi, D. Bersani, P. Paolo Lottici, Raman fingerprint of chromate, aluminate and ferrite spinels, *J. Raman Spectrosc. 46* (2015) 1255-1264.

[61] A.S. Madhusudhan Rao, K. Narender, Studies on thermophysical properties of CaO and MgO by γ-ray attenuation, *J. Thermodyn.* (2014) Article ID 123478.

[62] K. Haarmann, J.C. Vaillant, B. Vandenberghe, W. Bendick, A. Arbab, *The T91/P91 book*, Vallourec and Mannesmann tubes, Boulogne (2002).

[63] S. Wang, X. Liu, Y. Fei, Q. He, H. Wang, In situ high-temperature powder X-ray diffraction study on the spinel solid solutions $(Mg_{1-x}Mn_x)Cr_2O_4$, *Phys. Chem. Minerals 39* (2012) 189-198.

[64] A.V. Abramov, K.V. Dedov, A.F. Gibadullina, A.Y. Zhilyakov, V.V. Karpov, V.A. Volkovich, I.B. Polovov, Corrosive resistance of nickel Hastelloy G-35 superalloy in various aggressive media, *ECS Transactions 86* (2018) 155-162.

[65] A.V. Abramov, V.V. Karpov, A.Yu Zhilyakov, A.F. Gibadullina, I.B. Polovov, V.A. Volkovich, S.V. Belikov, A.V. Shak, O.I. Rebrin, Corrosion of corrosion-resistant and high-temperature nickel-based alloys in chloroaluminate melts, *ECS Transactions 64* (2014) 217-226.

[66] T.J. Lewis, A.J. Wright, The electrical conductivity of magnesium oxide at low temperatures, *J. Phys. D: Appl. Phys. 1* (1968) 441-447.

[67] R. Bender, M. Schütze, The role of alloying elements in commercial alloys for corrosion resistance in oxidizing-chloridizing atmospheres. Part I: Literature evaluation and thermodynamic calculations on phase stabilities, *Mater. Corr. 54* (2003) 567-586.

[68] S. Zhang, H. Li, Z. Jiang, B. Zhang, Z. Li, J. Wu, H. Feng, H. Zhu, F. Duan, Chloride- and sulphate-induce hot corrosion mechanism of super austenitic stainless steel S13254 under dry gas environment, *Corr. Sci. 163* (2020) 108295.

[69] H. Lux, «Saüren» und «Basen» im schmelzfluss: die Bestimmung der sauerstoffionen-konzentration, *Z. Elektrochem. 45* (1939) 303-309.

[70] H. Flood, T. Förland, The acidic and basic properties of oxides, *Acta Chem. Scand. 1* (1947) 592-604.

[71] Y-S. Hwang, R.A. Rapp, Synergistic dissolution of oxides in molten sodium sulfate, *J. Electrochem. Soc. 137* (1990) 1276-1280.

[72] R.A. Rapp, Y.S. Zhang, Hot corrosion of materials: fundamental studies, *JOM 46* (1994) 47-55.

[73] Y. Parsa, L. Latu-Romain, Y. Wouters, S. Mathieu, T. Perez, M. Vilasi, Effect of oxygen partial pressure on the semiconducting properties of thermally grown chromia on pure chromium, *Corr. Sci. 141* (2018) 46-52.

[74] A. Petric, H. Ling, Electrical conductivity and thermal expansion of spinels at elevated temperatures, *J. Am. Ceram. Soc. 90* (2007) 1515-1520.

[75] Z.F. Peng, S. Liu, C. Yang, F.Y. Chen, F.F. Peng, The effect of phase parameter variation on hardness of P91 components after service exposures at 530-550°C, *Acta Materialia 143* (2018) 141-155.

[76] M. Kowaka, H. Nagano, T. Kudo, Y. Okada, M. Yagi, O. Takaba, T. Yonezawa, K. Arioka, Effect of heat treatment on the susceptibility to stress corrosion cracking of Alloy 600, *J. Nucl. Technol. 55* (1981) 394-404.

[77] J.J. Kai, C.H. Tsai, T.A. Huang, M.N. Liu, The effects of heat treatment on the sensitization and SCC behavior of Inconel 600 alloy, *Metall. Trans. A 20* (1989) 1077-1088.

[78] E.L. Hall, C.L. Briant, The microstructural response of mill-annealed and solution-annealed Inconel 600 to heat treatment, *Metall. Trans. A 16* (1985) 1225-1236.

[79] B.S. Berry, Diffusion of carbon in nickel, *J. Appl. Phys. 44* (1973) 3792-3793.

[80] S.P. Murarka, M.S. Anand, R.P. Agarwala, Diffusion of chromium in nickel, *J. Appl. Phys. 35* (1964) 1339-1341.

[81] M. Zhu, H. Ma, M. Wang, Z. Wang, A. Sharif, Effects of cations on corrosion of Inconel 625 in molten chloride salts, *High Temp. Mater. Proc. 35* (2016) 337-345.

[82] G.F. Imbusch, A.L. Schawlow, A.D. May, S. Sugano, Fluorescence of MgO:Cr^{3+} ions in noncubic sites, *Phys. Rev. 140* (1965) A830-A838.

[83] M.B. O'Neill, B. Henderson, Site-selective laser spectroscopy of energy transfer in MgO:Cr^{3+}, *J. Luminescence 39* (1988) 161-166.

[84] S.P. Feofilov, A.B. Kulinkin, A.K. Kaveev, N.S. Sokolov, S.M. Suturin, Fluorescence spectroscopy of Cr^{3+} ions in MgO nanofilms on Al2O3 and GaN substrates, *Opt. Mater. 83* (2018) 43-46.

[85] D. Bachiller Perea, Ion-irradiation-induced damage in nuclear materials: Case study of a-SiO_2 and MgO, Doctoral Thesis accepted by the Université Paris-Sud and the Universidad Autónoma de Madrid, Springer Theses (2018) page 166.

[86] N.S. Awwad, A.M. Alshahrani, K.A. Saleh, M.S. Hamdy, A novel method to improve the anticancer activity of natural-based hydroxyapatite against the liver cancer cell line HepG2 using mesoporous magnesia as a micro-carrier, *Molecules 22* (2017) 1947-1-11.

[87] C.-L. Jiang, W. Zeng, F.-S. Liu, B. Tang, Q.-J. Liu, First-principles analysis of vibrational modes of calcite, magnesite and dolomite, *J. Phys. Chem. Solids 131* (2019) 1-9.

[88] K. Sasaki, S. Moriyama, Effect of calcination temperature for magnesite on interaction of MgO-rich phases with boric acid, *Ceram. Int. 40* (2014) 1651-1660.